



Axisymmetric ring solutions of the 2D Gray–Scott model and their destabilization into spots

David S. Morgan^a, Tasso J. Kaper^{b,*}

^a *Nonlinear Dynamical Systems Section, US Naval Research Laboratory, Washington, DC 20375, USA*

^b *Department of Mathematics and Center for BioDynamics, Boston University, Boston, MA 02215, USA*

Received 25 May 2003; received in revised form 21 October 2003; accepted 23 December 2003

Communicated by A. Doelman

Abstract

This article concerns annular ring solutions of the Gray–Scott model. In the monostable regime, annular rings are far-from-equilibrium patterns supported on annuli inside of which the activator is concentrated. The diffusive flux of inhibitor over long length scales toward such an annulus feeds the production of activator there, and the interaction is semi-strong. Numerical and experimental observations show that annular rings often split into spots, and the main result presented in this article is a method to predict the number of spots that an annular ring, unstable to angular disturbances, will split into. This method is an extension to 2D circular geometries of the nonlocal eigenvalue problem (NLEP) method developed for pulse solutions of the 1D Gray–Scott problem, in which the full eigenvalue problem—a pair of second-order, nonautonomous coupled equations—is recast as a single, second-order equation with a nonlocal term. We also continue the results for the monostable regime into the bistable regime of the Gray–Scott model, where target patterns exist and their rings are observed to destabilize into rings of spots, as may be shown using a classical Turing/Ginzburg–Landau analysis. Thus, for these 2D circular geometries, the NLEP method is to the instability of annular rings in the monostable regime what the Turing analysis is to the instability of target patterns in the bistable regime near criticality.

© 2004 Elsevier B.V. All rights reserved.

Keywords: 2D Gray–Scott model; Nonlocal eigenvalue problem; Turing analysis; Annular rings; Spots

1. Introduction

The Gray–Scott model [17,18] is a prototypical cubic autocatalysis system that exhibits a striking array of patterns, many of which have been discovered approximately 10 years ago [23–25,38,40]. The governing equations are

$$\frac{\partial U}{\partial t} = D_U \Delta U - UV^2 + A(1 - U), \quad \frac{\partial V}{\partial t} = D_V \Delta V + UV^2 - BV. \quad (1.1)$$

Here $U = U(x, t)$ and $V = V(x, t)$ are the concentrations of the inhibitor U and the activator V , $x \in \mathbb{R}^2$, Δ is the Laplace operator, D_U and D_V are the diffusivities (with $D_U > D_V$), and A and B are positive rate constants.

* Corresponding author. Tel.: +1-617-353-9552; fax: +1-617-353-8100.

E-mail address: tasso@math.bu.edu (T.J. Kaper).

Recent analytical studies have focused on spots in two dimensions and pulses in one dimension [6–12,27,28,30,31,35,36,41,44–46]. Spots and pulses can undergo a process called self-replication. For spots, self-replication is visually similar to cell division in that an initially radially symmetric spot elongates into a peanut shape and then splits into two spots, with the pinch off occurring along a line perpendicular to the direction of elongation. For pulses, self-replication involves a parent pulse splitting into two daughter pulses when either the central peak of the pulse collapses (stationary splitting) or a new peak forms at or near the inflection point along the trailing edge (dynamic splitting). Moreover, the further evolution of the two daughter spots or pulses may be to any number of other patterns, including further self-replication into 4, 8, . . . spots or pulses, stationary arrays of spots or pulses, and in 2D also lamellar patterns, annular rings, phase turbulence, and others, see [20,25,37].

Recent experiments and numerical simulations have also revealed an interesting interplay between spots and annular rings. On the one hand, an annular ring is created when the central peak of a spot collapses. On the other hand, annular rings are observed to break up into rings of spots, in certain overlapping parameter regimes.

In this article, which presents results from [28], we study annular rings and spots of Eq. (1.1) on a disk of radius r_{\max} in the monostable regime, $A < 4B^2$, where $(U = 1, V = 0)$ is the only homogeneous steady state. These patterns are localized patterns for which the activator concentration is significant only inside some domain—an annulus for the rings and a disk for the spots. Moreover, the inhibitor concentration is, to a first approximation, constant over these same domains, while it increases back to $U = 1$ over long length scales. Therefore, the interaction between the activator and the inhibitor is semi-strong, just as it is in [12], for example.

We use matched asymptotics to construct these patterns. The inner (or fast) region is the localized annulus of central radius R , determined uniquely by r_{\max} and the other physical parameters, and of narrow-width, $\mathcal{O}(\sqrt{D/B})$, such that on each ray of constant angle emanating from the origin the cross-section of the localized ring is to leading order a pulse, or homoclinic orbit, centered on $r = R$. The outer (or slow) regions are the disk interior to the annulus ($0 \leq r < R$) and the exterior domain ($R < r \leq r_{\max}$), over which U varies slowly. Matching [15] of the inner and outer solutions is then carried out at the edges of the annulus, and this matching determines U_0 , the local minimum of the inhibitor concentration at $r = R$, and hence also the height of the ring itself, i.e. V_{\max} . These matching results are shown to agree quantitatively with the results from numerical simulations of the radially symmetric version of Eq. (1.1).

Next, we examine the linearized stability of these pulse-type annular ring solutions on long, but not infinitely long, time scales. Our main goal is to identify parameter regimes in which there exists a discrete set of angular wave numbers, m , such that, on long but $\mathcal{O}(1)$ time scales, a ring is unstable to disturbances of angular wavelength $2\pi/m$. In these regimes, one expects an annular ring solution to split into m spots.

The full eigenvalue problem, consisting of two, coupled, second-order equations, inherits the inner–outer (or fast–slow) structure from the annular ring solution, with the eigenfunction component corresponding to the activator concentration being fast and the eigenfunction component corresponding to the inhibitor being slow. This full eigenvalue problem can be reduced either by encoding the dynamics of the slow component in the fast equation or by encoding the dynamics of the fast component into the slow equation. We choose the former approach and derive a single, second-order equation for the fast eigenfunction component that includes a nonlocal term containing information about the slow component. This equation turns out to be an inhomogeneous hypergeometric equation; and, because the reduced equation is nonlocal, the method has been called the nonlocal eigenvalue problem method, or NLEP method, for short, see [8–10,13]. The NLEP method has been found to be useful for pulse solutions which can have $\mathcal{O}(1)$ unstable eigenvalues, and it has also been used to find small eigenvalues, see for example [9]. The other choice of reduction (encoding the fast dynamics in the slow eigenfunction equation) is made in the singular limit eigenvalue problem (SLEP) method, see [33], and it has been shown to be useful for fronts in bistable systems and when small eigenvalues (which vanish in the limit of zero interfacial thickness) are of concern.

The coupling from the slow field into the equation of the fast eigenfunction component is the mechanism responsible for stabilizing the localized solutions of high activator concentration. With the NLEP method, one quantifies the strength of this coupling and, hence, one can study how the eigenvalues change as the parameters change. For example, for pulses in one space dimension in the Gray–Scott model, where there can be $\mathcal{O}(1)$ unstable eigenvalues, a subcritical Hopf bifurcation occurs in which the pulse solutions become stable [8,10], and see also [7].

In the 2D problem under consideration here, this coupling also depends on the angular wave number, m , associated to angular disturbances. Hence, we may use the extension of the NLEP method to derive the main results of the paper, namely, the intervals of values of m for which unstable eigenvalues and nontrivial, bounded eigenfunction pairs exist. Numerical simulations confirm the validity, both qualitatively and quantitatively, of the NLEP predictions, since the most unstable wave numbers correspond exactly to the number of spots into which rings are observed to split.

The above analysis of the annular rings and spots in the monostable regime is complemented by a (brief) analysis in the bistable regime ($A > 4B^2$, see [27]). Specifically, a classical Turing/Ginzburg–Landau analysis (see, e.g. [16,42] and the more modern presentation in [14]) in the bistable regime shows how target patterns and hexagons arise at critical parameter values from the linearly unstable, homogeneous state. We identify the critical bifurcation parameter and show that the associated critical angular wave numbers correspond to the number of spots observed along the rings of the target patterns.

Finally, we show how the patterns observed in the monostable and bistable regimes may be connected to each other via a continuation in parameter space. The singular, large-amplitude structures present in the monostable regime, where the perturbations must be large since the background state is linearly stable, become small-amplitude disturbances of the unstable state in the bistable regime. Therefore, from the point of view of the stability analysis, the NLEP method is to the instability of rings in the monostable regime what the Turing analysis is to instability of rings in the bistable regime near criticality.

All of the numerical simulations carried out for this study used the codes presented in [1,2]. Details are given below.

Annular ring solutions have been studied in other problems, mainly in bistable systems [5,22,26,32]. There, the solutions are near one stable, homogeneous state inside the annulus and near a second, distinct, stable, homogeneous state outside the annulus; and, these two states are connected via heteroclinic orbits (a.k.a. domain walls). See especially [26] for a study of how annular rings in excitable, bistable systems can break up and [34] for a general study of interfaces in singularly perturbed bistable systems. See also [4] for an interesting example of radially symmetric solutions in a model from phase field theory.

This article is organized as follows. In Section 2, the construction of the annular ring solutions in the monostable regime is presented. The linear stability study and the analysis of their deformation into spots are given in Section 3. Then, Section 4 contains the brief evaluation of the Turing/Ginzburg–Landau bifurcation point in the bistable regime, as well as the continuation of these “classical” patterns to the monostable regime. Finally, some related phenomena, including ring splitting, are discussed in Section 5.

2. Annular ring solutions

In this section, we set $D_U = 1$ and $D_V = D \ll 1$ and construct stationary axisymmetric annular ring solutions for $r \in [0, r_{\max}]$ of the system:

$$\frac{\partial^2 U}{\partial r^2} + \frac{1}{r} \frac{\partial U}{\partial r} = UV^2 - A + AU, \quad D \left(\frac{\partial^2 V}{\partial r^2} + \frac{1}{r} \frac{\partial V}{\partial r} \right) = -UV^2 + BV \quad (2.1)$$

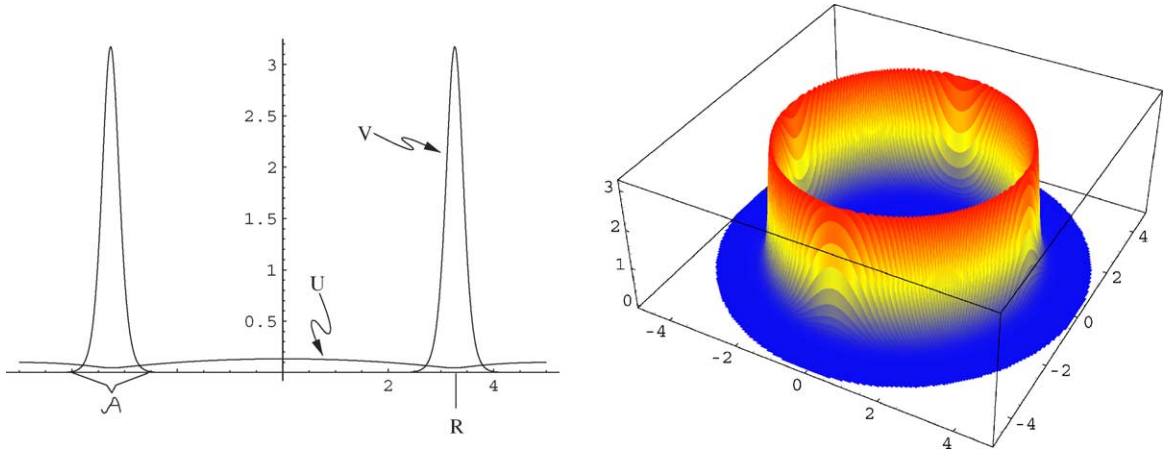


Fig. 1. The left figure is a cross-section of the U and V components of an annular solution of interest, with the annular region \mathcal{A} and the radius R indicated. The right figure presents a 3D view of the V component of an annular ring solution which has the appearance of a volcano crater. For both figures, the parameter values are $A = 0.04$, $B = 0.102$, $D = 0.001$, $r_{\max} = 5$, $R \approx 3.26$.

with boundary conditions:

$$U_r(0), U_r(r_{\max}), V_r(0), V_r(r_{\max}) = 0. \quad (2.2)$$

For such solutions there is a narrow annular ring \mathcal{A} of central radius R , where the value of R is determined by physical parameters, as shown below, and where the solution V is of width $\mathcal{O}(\sqrt{D/B})$ at half height. On the annulus \mathcal{A} , the activator concentration V exhibits a pulse-type profile with a maximum at $r = R$, while the inhibitor concentration U is essentially flat near its minimum. Outside of \mathcal{A} , V vanishes exponentially, while U is slowly increasing. Thus, in the 3D (r, θ, V) space, V takes on the appearance of a ‘volcano’ with a deep circular crater (see Fig. 1). Given these observations, we analyze (2.1) separately inside \mathcal{A} , on \mathcal{A} , and outside of \mathcal{A} and then match the results. This procedure follows that used in [6] for 1D pulses.

2.1. Leading order fast solution for V

We change variables to $\xi = r - R$, so that ξ is centered on \mathcal{A} , and it is also useful to introduce a stretched version of ξ , namely

$$\hat{\xi} = \sqrt{\frac{B}{D}} \xi,$$

since the pulse width is $\mathcal{O}(\sqrt{D/B})$. Let U_0 denote the (as yet unknown) value of U at $\xi = 0$. Numerical simulations show that the maximum of V scales inversely with U_0 , so we set

$$\hat{V}(\hat{\xi}) = \frac{U_0}{B} V(\xi). \quad (2.3)$$

In addition, numerical simulations reveal that U is approximately constant (U_0) on \mathcal{A} . These scalings and observations lead us to rewrite the equation for V as

$$\frac{\partial^2 \hat{V}}{\partial \hat{\xi}^2} + \hat{V}^2 - \hat{V} = \left(\frac{U_0 - U}{U_0} \right) \hat{V}^2 - \frac{1}{\hat{\xi} + \sqrt{B/DR}} \frac{\partial \hat{V}}{\partial \hat{\xi}} \quad (2.4)$$

with boundary conditions:

$$\hat{V}_{\hat{\xi}}|_{\hat{\xi}=-R/\sqrt{D/B}}, \quad \hat{V}_{\hat{\xi}}|_{\hat{\xi}=(r_{\max}-R)/\sqrt{D/B}} = 0. \quad (2.5)$$

We assume that

$$\sqrt{\frac{B}{D}} \gg 1 \quad (2.6)$$

and that, on \mathcal{A} :

$$U - U_0 \ll 1.$$

Hence, the right member of (2.4) is a small perturbation. While there might appear to be a singularity in the right member of (2.4) as $\hat{\xi} \rightarrow -R\sqrt{B/D}$, $\hat{V}_{\hat{\xi}}$ decays exponentially as $\hat{\xi} \rightarrow -R\sqrt{B/D}$, the right-hand member vanishes. The leading order equation for V on \mathcal{A} is then

$$\hat{V}_0'' + \hat{V}_0^2 - \hat{V}_0 = 0. \quad (2.7)$$

Moreover, the boundary conditions are

$$\hat{V}_0(\hat{\xi}) \rightarrow 0 \quad \text{exponentially as } |\hat{\xi}| \rightarrow \infty \quad (2.8)$$

and the solution of (2.7) that satisfies (2.8) is the homoclinic loop:

$$\hat{V}_0(\hat{\xi}) = \frac{3}{2} \operatorname{sech}^2\left(\frac{1}{2}\hat{\xi}\right). \quad (2.9)$$

Remark. The full problem (1.1) is to be solved on a finite domain, while the above boundary conditions are at infinity. This approach is standard in asymptotic analysis and is justified since the homoclinic solution approaches the saddle $\{V = 0, V' = 0\}$ exponentially fast as $\hat{\xi} \rightarrow \pm\infty$. Thus, only an exponentially small error is introduced in considering the infinite tails.

Next, we derive conditions on the parameters under which the assumption that U is constant to leading order on \mathcal{A} holds. Substituting (2.3) into the first equation of (2.1), with the additional scaling $U = U_0\hat{U}$, one obtains to leading order:

$$\hat{U}_{\hat{\xi}\hat{\xi}} = \frac{BD}{U_0^2}\hat{U}\hat{V}^2 - \frac{AD}{BU_0} + \frac{AD}{B}\hat{U}. \quad (2.10)$$

Thus, since \hat{U} is bounded as $\hat{\xi} \rightarrow \pm\infty$, \hat{U} is constant to leading order on \mathcal{A} , provided that

$$\frac{BD}{U_0^2} \ll 1, \quad \frac{AD}{BU_0} \ll 1, \quad \frac{AD}{B} \ll 1. \quad (2.11)$$

We will show that $U_0 \ll 1$ (see (2.24)), so that the second condition implies the third and hence, only the first two conditions are needed. The first derivative term $U_{\hat{\xi}}$ from (2.1) is of higher order in the scaled variables; specifically, it is

$$\frac{-\hat{U}_{\hat{\xi}}}{\hat{\xi} + \sqrt{B/DR}}$$

and we recall $\sqrt{B/DR} \gg 1$.

2.2. Leading order slow solution for U

In this section, we obtain approximations of the solution U inside and outside of \mathcal{A} , where V is exponentially small. We first rewrite the equation for U as a linear equation and treat the nonlinear term UV^2 as an inhomogeneous quantity:

$$L[U] \equiv \frac{\partial^2 U}{\partial r^2} + \frac{1}{r} \frac{\partial U}{\partial r} - AU = UV^2 - A \quad (2.12)$$

with the boundary conditions:

$$U_r(0), \quad U_r(r_{\max}) = 0. \quad (2.13)$$

The unique solution of $L[U] = -A$ satisfying the given boundary conditions is $U \equiv 1$. Next, the problem

$$L[U] = UV^2 \quad (2.14)$$

with the boundary conditions (2.13), can be solved using a Greens function. Hence, the solution for the full problem (2.12) with the boundary conditions (2.13) is

$$U(r) = 1 - \left[\kappa I_0(\sqrt{Ar}) \int_0^{r_{\max}} I_0(\sqrt{As}) s U(s) V^2(s) ds + K_0(\sqrt{Ar}) \int_0^r I_0(\sqrt{As}) s U(s) V^2(s) ds + I_0(\sqrt{Ar}) \int_r^{r_{\max}} K_0(\sqrt{As}) s U(s) V^2(s) ds \right], \quad (2.15)$$

where I_0 and K_0 are the modified Bessel functions of first and second kind, and

$$\kappa = \frac{K_1(\sqrt{Ar_{\max}})}{I_1(\sqrt{Ar_{\max}})}. \quad (2.16)$$

Now, it follows from (2.3), (2.7) and (2.9) that V is essentially zero away from an $\mathcal{O}(\sqrt{D/B})$ neighborhood of $r = R$ ($\xi = 0$). By approximating $I_0(\sqrt{Ar})r$ and $K_0(\sqrt{Ar})r$ with their values at $r = R$ and using the fact that U is constant to leading order in an $\mathcal{O}(\sqrt{D/B})$ neighborhood of $r = R$, one obtains the following leading order approximation for U :

$$U(r) = 1 - \left[\kappa I_0(\sqrt{Ar}) I_0(\sqrt{AR}) R U_0 \int_0^{r_{\max}} V^2(s) ds + K_0(\sqrt{Ar}) I_0(\sqrt{AR}) R U_0 \int_0^r V^2(s) ds + I_0(\sqrt{Ar}) K_0(\sqrt{AR}) R U_0 \int_r^{r_{\max}} V^2(s) ds \right]. \quad (2.17)$$

Thus, given the (as yet unknown) quantities R and U_0 , Eq. (2.17) governs the leading order behavior of U . We will derive expressions for U_0 and R in Sections 2.3 and 2.5, respectively, and use the approximation (2.9) for V .

2.3. Determination of U_0

We now determine $U_0 \equiv U(r = R)$. Evaluating (2.17) at $r = R$, we find

$$U_0 = 1 - U_0 [\kappa I_0^2(\sqrt{AR}) R + I_0(\sqrt{AR}) K_0(\sqrt{AR}) R] \int_0^{r_{\max}} V^2(s) ds. \quad (2.18)$$

Using (2.3) and (2.9) and performing a straightforward integration, we have to leading order:

$$\int_0^{r_{\max}} V^2(s) ds = \frac{B^{3/2} \sqrt{D}}{U_0^2} \int_{-\infty}^{\infty} \hat{V}^2(\hat{\xi}) d\hat{\xi} = \frac{6B^{3/2} \sqrt{D}}{U_0^2}. \quad (2.19)$$

Combining this with (2.18), we find

$$U_0(1 - U_0) = \frac{6B^{3/2}\sqrt{D}}{\sqrt{A}}L, \quad (2.20)$$

where

$$L = \kappa I_0^2(\sqrt{A}R)\sqrt{A}R + I_0(\sqrt{A}R)K_0(\sqrt{A}R)\sqrt{A}R. \quad (2.21)$$

Eq. (2.20) is quadratic, with two real solutions:

$$(U_0)_\pm = \frac{1}{2} \left(1 \pm \sqrt{1 - \frac{24B^{3/2}\sqrt{D}}{\sqrt{A}}L} \right), \quad (2.22)$$

as long as

$$\frac{6B^{3/2}\sqrt{D}}{\sqrt{A}} < \frac{1}{4L}. \quad (2.23)$$

We focus our attention on the regime $B^{3/2}/\sqrt{A} < \mathcal{O}(1/\sqrt{D})$, in which the solutions are observed numerically. Here, $(U_0)_+$ is a small perturbation of the linearly stable homogeneous solution $U \equiv 1$, and hence an annular ring solution with $U_0 = (U_0)_+$ is not expected to be stable, even on relatively short time scales. In contrast, $(U_0)_-$ is to leading order:

$$(U_0)_- = \frac{6B^{3/2}\sqrt{D}}{\sqrt{A}}L \ll 1 \quad (2.24)$$

and so we focus on annular ring solutions with this value of U_0 for the remainder of this section. There is a saddle-node bifurcation of annular ring solutions when

$$\frac{6B^{3/2}\sqrt{D}}{\sqrt{A}} = \frac{1}{4L},$$

in which the two solutions constructed here merge.

Remark. A further word is in order about the relative sizes of the small terms in the leading order U equation, (2.10). We had assumed, see (2.11), that $BD/U_0^2 \ll 1$ and $AD/BU_0 \ll 1$, and verified that these conditions are satisfied for the simulations in which annular rings of the type we analyze here occur. It turns out that the first small term dominates the second. Recall (2.24), $(U_0)_- = (6B^{3/2}\sqrt{D}/\sqrt{A})L$, to leading order. Hence, to leading order, $BD/U_0^2 = A/36L^2B^2$ and $AD/BU_0 = A^{3/2}\sqrt{D}/6LB^{5/2}$, and the condition that the first term dominates the second is therefore

$$6L\sqrt{\frac{AD}{B}} \ll 1.$$

This condition holds in our simulations. For example, for the parameter sets used in the left and right frames of Fig. 4, $6L\sqrt{AD/B} \approx 0.17, 0.10$, respectively. This relative ordering of the small terms is important for the construction and the stability of the annular ring solutions. In the inner fast domain, V is nontrivial and, hence, the dominant contribution to the jump discontinuity, $\Delta_{\hat{\xi}}\hat{U}$, in \hat{U} comes from the first small term and is proportional to $\int_{-\infty}^{\infty} \hat{U}\hat{V}^2 d\hat{\xi}$.

Table 1

The results of the approximation of (2.27) using numerical data from simulations of the radially symmetric Gray–Scott problem^a

D	Value of lhs of (2.27)
10^{-2}	0.043
10^{-3}	0.011
10^{-4}	0.0033
10^{-5}	0.001
10^{-6}	0.00031

^a In all simulations, $A = 0.08$, $B = 0.2$, and $r_{\max} = 5$.

2.4. Analytic perturbation theory for the fast solution of V

We now derive the solvability (or Melnikov) condition for the equation governing the existence of annular ring solutions. For the remainder of this article we drop hats on all variables, unless otherwise mentioned. Multiplying (2.7) by $\partial V/\partial \xi$, one obtains

$$\frac{\partial}{\partial \xi} H(V, V') = \frac{-1}{\xi + \sqrt{B/DR}} \left(\frac{\partial V}{\partial \xi} \right)^2 + \frac{\partial}{\partial \xi} \left[\frac{U}{U_0} \right] \frac{V^3}{3}, \quad (2.25)$$

where

$$H(V, V') = \frac{1}{2} \left(\frac{\partial V}{\partial \xi} \right)^2 + \frac{U}{3U_0} V^3 - \frac{1}{2} V^2 \quad (2.26)$$

is the Hamiltonian of the system $V'' + (U/U_0)V^2 - V = 0$. Carrying out a leading order analysis in the limit $D \rightarrow 0$, we find by integrating both sides of (2.25) and recalling that $\hat{V}(\hat{\xi})$ decays exponentially that

$$- \int_{-\infty}^{\infty} \frac{1}{\xi + \sqrt{B/DR}} \left(\frac{\partial V}{\partial \xi} \right)^2 d\xi + \frac{1}{3} \int_{-\infty}^{\infty} \frac{\partial}{\partial \xi} \left(\frac{U}{U_0} \right) V^3 d\xi = 0. \quad (2.27)$$

This equation, therefore, is a natural condition for the existence of an axisymmetric solution to (1.1). As an added check we evaluated this expression numerically using data from simulations and found good agreement with the leading order theory. See Table 1 for the results.

The second term on the left-hand side of (2.27) can be simplified by observing that, to leading order:

$$\frac{\partial}{\partial \xi} \left(\frac{U}{U_0} \right) = \left[\frac{\partial}{\partial \xi} \left(\frac{U}{U_0} \right) \right]_{\xi=0} + \tilde{h}(\xi), \quad (2.28)$$

where $\tilde{h}(\xi)$ is (locally) an odd function about $\xi = 0$. We show this as follows, and the reader who wishes to skip this part on the first reading may go directly to the last paragraph of this section. Up to the last paragraph of this section, we reintroduce hats on the appropriate variables.

Taking the derivative of (2.17), one gets to leading order:

$$\frac{\partial}{\partial \hat{\xi}} \left[\frac{U}{U_0} \right] = \sqrt{\frac{D}{B}} \frac{\partial}{\partial \xi} \left[\frac{U}{U_0} \right], \quad (2.29)$$

$$\frac{\partial}{\partial \hat{\xi}} \left[\frac{U}{U_0} \right] \sim \sqrt{\frac{D}{B}} \left[-Q_0 \int_0^{r_{\max}} V^2(s) ds + Q_1 \int_0^{\hat{\xi}+R} V^2(s) ds - Q_2 \int_{\hat{\xi}+R}^{r_{\max}} V^2(s) ds \right], \quad (2.30)$$

where

$$\begin{aligned} Q_0 &= \kappa I_0(\sqrt{AR}) I_1(\sqrt{AR}) \sqrt{AR}, & Q_1 &= I_0(\sqrt{AR}) K_1(\sqrt{AR}) \sqrt{AR}, \\ Q_2 &= I_1(\sqrt{AR}) K_0(\sqrt{AR}) \sqrt{AR}. \end{aligned} \tag{2.31}$$

Next, we change variables $\xi \rightarrow \hat{\xi}$, $V \rightarrow \hat{V}$ in the integrals. Also, we use that, to leading order, $\int_{-R}^c \hat{V}^2(\hat{\xi}) d\hat{\xi} = \int_{-\infty}^c \hat{V}^2(\hat{\xi}) d\hat{\xi}$ and $\int_c^{r_{\max}} \hat{V}^2(\hat{\xi}) d\hat{\xi} = \int_c^{\infty} \hat{V}^2(\hat{\xi}) d\hat{\xi}$, since \hat{V} decays at an exponential rate away from $\hat{\xi} = 0$. Hence, the tails $\int_{-\infty}^{-R} \hat{V}^2(\hat{\xi}) d\hat{\xi}$ and $\int_{r_{\max}}^{\infty} \hat{V}^2(\hat{\xi}) d\hat{\xi}$ are of higher order and introduce only an exponentially small error. We can rewrite (2.30) as

$$\begin{aligned} \frac{\partial}{\partial \hat{\xi}} \left[\frac{U}{U_0} \right] &= \frac{BD}{U_0^2} \left[-Q_0 \int_{-\infty}^{\infty} \hat{V}^2 d\hat{\xi} + \frac{1}{2} (Q_1 - Q_2) \int_{-\infty}^{\infty} \hat{V}^2 d\hat{\xi} \right. \\ &\quad \left. + \frac{1}{2} (Q_1 + Q_2) \left(\int_{-\infty}^{\sqrt{D/B\hat{\xi}}} \hat{V}^2(s+R) ds - \int_{\sqrt{D/B\hat{\xi}}}^{\infty} \hat{V}^2(s+R) ds \right) \right], \end{aligned} \tag{2.32}$$

by adding and subtracting:

$$\int_{\sqrt{D/B\hat{\xi}}}^{\infty} \hat{V}^2 d\hat{\xi}$$

to the terms involving Q_1 and Q_2 . By rearranging terms and using the fact that $Q_1 + Q_2 = 1$, we arrive at an expression of the form (2.28):

$$\frac{\partial}{\partial \hat{\xi}} \left[\frac{U}{U_0} \right] \sim \frac{BD}{2U_0^2} \left[(-2Q_0 + Q_1 - Q_2) \int_{-\infty}^{\infty} \hat{V}^2(s) ds + \tilde{h}(\hat{\xi}) \right], \tag{2.33}$$

where

$$\tilde{h}(\hat{\xi}) = \left[\int_{-\infty}^{\sqrt{D/B\hat{\xi}}} \hat{V}^2(s+R) ds - \int_{\sqrt{D/B\hat{\xi}}}^{\infty} \hat{V}^2(s+R) ds \right]$$

is an odd function about $\hat{\xi} = 0$.

We again drop hats for the remainder of the calculations. Substituting (2.33) into (2.27), we obtain to leading order the simplified condition:

$$-\frac{1}{R} \sqrt{\frac{D}{B}} \int_{-\infty}^{\infty} \left(\frac{\partial V_0}{\partial \xi} \right)^2 d\xi + \frac{1}{3} \left[\frac{\partial}{\partial \xi} \left(\frac{U}{U_0} \right) \right]_{\xi=0} \int_{-\infty}^{\infty} V_0^3(\xi) d\xi = 0. \tag{2.34}$$

Substitution of (2.9) for V_0 and (2.33) for $[(\partial/\partial \xi)(U/U_0)]_{\xi=0}$ into (2.34) and two straightforward integrations yield the following leading order condition for the existence of stationary axisymmetric solutions:

$$-\frac{1}{R} \sqrt{\frac{D}{B}} + \frac{6BD}{U_0^2} (-2Q_0 + Q_1 - Q_2) = 0. \tag{2.35}$$

Eq. (2.35) involves A, B, D, R and r_{\max} and, thus, determines the value of R .

2.5. Completion of the existence analysis

Substituting $U_0 = (U_0)_-$ from (2.24) into (2.35), we find that annular ring solutions exist when

$$\mu = \frac{6B^{3/2} \sqrt{D}}{\sqrt{A}}, \tag{2.36}$$

where

$$\mu(\sqrt{AR}, \sqrt{Ar_{\max}}) \equiv \frac{2\sqrt{AR}}{L^2} \left[-Q_0 + \frac{1}{2}(Q_1 - Q_2) \right] \tag{2.37}$$

and we recall that $Q_0, Q_1,$ and Q_2 depend on \sqrt{AR} , and L depends on \sqrt{AR} and $\sqrt{Ar_{\max}}$. A straightforward asymptotic analysis of μ shows that $\mu \rightarrow \infty$ as $R \rightarrow 0$. Furthermore, $\mu < 0$ for $R = r_{\max}$. Moreover, μ is continuous in r , and the right-hand side of (2.36) is positive. Hence, given any set of positive parameters A, B and D , and any r_{\max} , there exists a real solution of (2.36) for R . We solve (2.36) numerically with Mathematica [47], since it involves Bessel functions in a nontrivial manner.

We require that (2.23) holds, since otherwise $(U_0)_-$ is not real. Combining (2.23) with (2.36), we thus find that axisymmetric solutions to (1.1) exist when

$$0 < \frac{2\sqrt{AR}}{L^2} \left[-Q_0 + \frac{1}{2}(Q_1 - Q_2) \right] < \frac{1}{4L}, \tag{2.38}$$

that is, when the graph of μ lies between the r -axis and the graph of $1/4L$. We can, without loss of generality by rescaling A , set $r_{\max} = 1$, since A occurs in the formula only via $\sqrt{Ar_{\max}}$ and \sqrt{AR} . Then μ depends only on A and R . We show below that there exists a value A_{bif} , such that when $A < A_{\text{bif}}$, the graph of μ lies below the graph of $1/4L$, and thus, for any pair of parameters (B, D) , there exists a valid solution of (2.36). When $A > A_{\text{bif}}$, there is an interval where the graph of μ lies above the graph of $1/4L$, and thus a valid solution of (2.36) exists only if

$$\frac{6B^{3/2}\sqrt{D}}{\sqrt{A}} > \mathcal{E}_+,$$

or

$$\frac{6B^{3/2}\sqrt{D}}{\sqrt{A}} < \mathcal{E}_-,$$

where \mathcal{E}_+ and \mathcal{E}_- are the abscissae of intersections of the graphs of μ and $1/4L$, as indicated in Fig. 2. The cases $A < A_{\text{bif}}$ and $A > A_{\text{bif}}$ are separated by a bifurcation at $A = A_{\text{bif}}$.

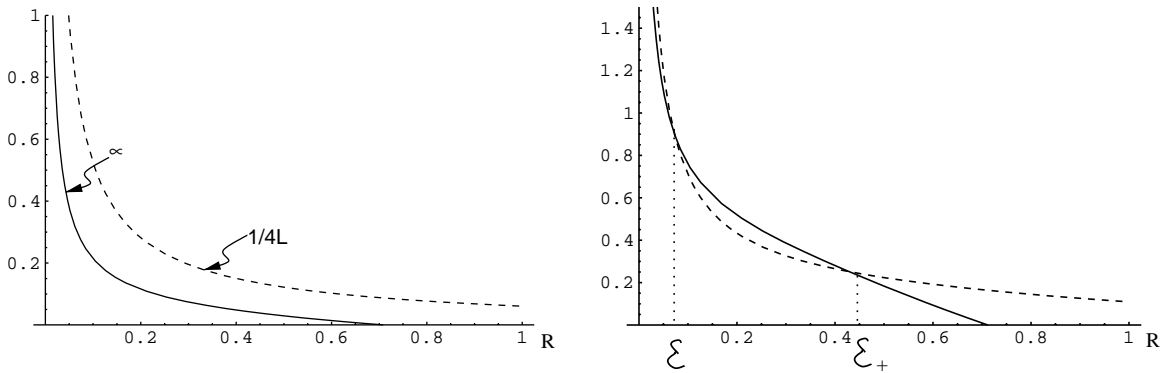


Fig. 2. These figures show the graphs of μ (2.37)—the solid curve—and $1/4L$ (2.21)—the dashed curve—as functions of R , for different values of A . In the left figure, $A = 0.25$, which is less than A_{bif} . In the right figure, $A = 0.95$, which is greater than A_{bif} . Annular ring solutions exist for a fixed R when the solid line is below the dashed line and above the R -axis. Thus, in the left figure, there are annular ring solutions for all $R \in (0, 0.71)$. As A increases through A_{bif} , this existence interval splits into two intervals.

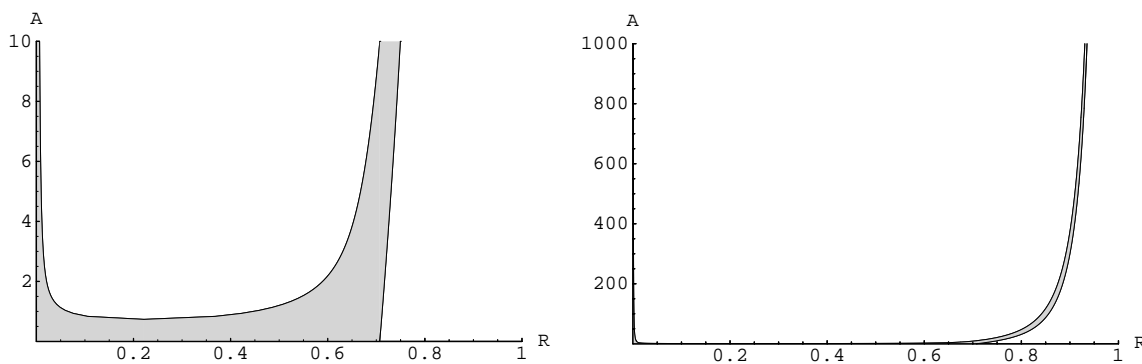


Fig. 3. The existence regime for annular ring solutions: the shaded region shows the R values such that an annular ring solution exists for a given A . For a fixed A , the value of R where such an annular ring solution is located is determined uniquely by B and D . As $A \rightarrow \infty$, the existence intervals narrow and approach 0 and r_{\max} . Note the scales on the vertical axes.

To determine the location of the bifurcation in A – R parameter space, there are two conditions:

$$\mu - \frac{1}{4L} \Big|_{A=A_{\text{bif}}, R=R_{\text{bif}}} = 0, \quad \frac{\partial}{\partial R} \left(\mu - \frac{1}{4L} \right) \Big|_{A=A_{\text{bif}}, R=R_{\text{bif}}} = 0,$$

where of course $0 < R < r_{\max}$ (Fig. 3). The second condition ensures that the graphs of μ and $1/4L$ meet tangentially. Using the Newton–Raphson method, we find

$$A_{\text{bif}} \sim 0.735176, \quad R_{\text{bif}} \sim 0.221469.$$

We graph μ and $1/4L$, the right-hand side of (2.23), in Fig. 2, for fixed values of A below and above A_{bif} .

2.6. Corroboration of analytical results: numerical simulations of the axisymmetric problem

In this section, we present the results of numerical simulations of the radially symmetric Gray–Scott problem, obtained using the adaptive grid code [2], to corroborate the analysis of the previous sections. Initial data was of the form:

$$U = 1.0 - \alpha \operatorname{sech}^2 \left(\frac{R-r}{\varepsilon_U} \right), \quad V = \beta \operatorname{sech}^2 \left(\frac{R-r}{\varepsilon_V} \right) \tag{2.39}$$

for fixed α , β , ε_U , ε_V , and where, for most simulations, we took $\alpha = 0.6$, $\beta = 1.4$ and $\varepsilon_U = \varepsilon_V = 0.25$. Eqs. (2.39) represent a large perturbation of U and V away from the background state $(U, V) = (1, 0)$, localized about $r = R$. Neumann boundary conditions $U_r(0, t) = U_r(r_{\max}, t) = 0$ and $V_r(0, t) = V_r(r_{\max}, t) = 0$ were used, and the simulations were run long enough for the solution to reach its asymptotic state. The results of two such simulations are shown in Fig. 4.

To further verify the analysis, we numerically approximate the exact Melnikov function given by the left-hand side of (2.27), using the results from simulations of the radially symmetric Gray–Scott problem. We evaluate the integrals on the left-hand side of (2.27) by the trapezoidal rule, while the derivatives V_ξ and U_ξ are computed using a standard central difference approximation. For a fixed set of parameters (A, B, r_{\max}) , we ran simulations for a collection of values of D from the set $\{10^{-2}, 10^{-3}, 10^{-4}, 10^{-5}, 10^{-6}\}$. Table 1 gives the results. The numerics agree well with the analysis.

In addition, we examined the evolution of initial data of the form (2.39) for fixed α , β , ε_U and ε_V , and where R , the location of the initial disturbance, was varied. For all $R < r_{\max}$, the solution evolved to the axisymmetric result

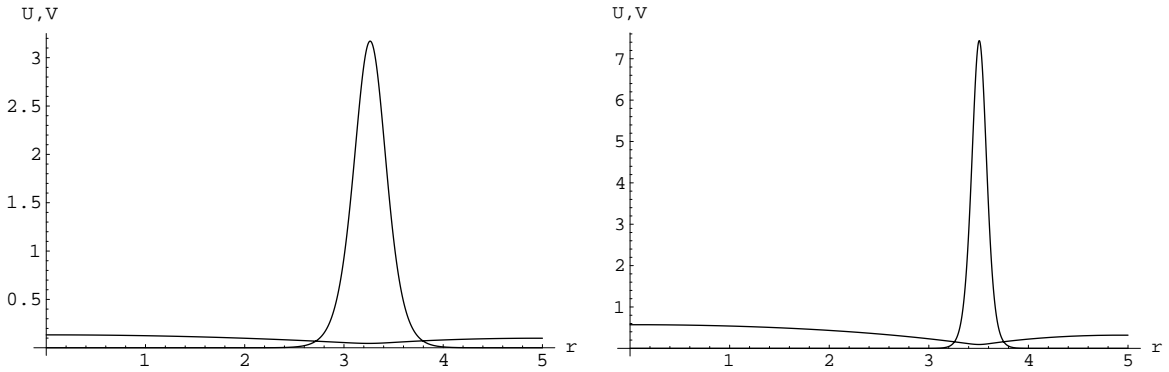


Fig. 4. Radial cross-sections of the annular ring solutions. In both of these simulations, $D = 0.001$ and $r_{\max} = 5$. In the left figure, the parameters are $A = 0.04$ and $B = 0.102$, while in the right figure, $A = 0.3$ and $B = 0.5$. The leading order theory predicts the existence of an annular ring solution with $R \approx 3.38$, $U_0 \approx 0.042$, $\sqrt{d}L \approx 0.13$ and $L \approx 1.42$ for the left figure, and $R \approx 3.62$, $U_0 \approx 0.083$, $\sqrt{d}L \approx 0.11$ and $L \approx 0.70$ for the right figure, where $d = B^2\sqrt{D}/A$ (see also Section 3.1). The actual location of the solutions are approximately $r = 3.26$ and 3.51 , while $U_0 \approx 0.045$ as calculated from simulation data for the left figure and $U_0 \approx 0.093$ as calculated for the right figure.

predicted by the analysis. For $R = r_{\max}$, the result was half of an annular solution, which obtained its maximum on the boundary of the domain (see Fig. 5).

Remark. The analysis of this section can be modified in a straightforward fashion to carry out a study using matched asymptotic expansions of these boundary solutions. We do not consider them further here.

Remark. The leading order scaled inhibitor equation (2.10) is exactly the same equation derived for U in the context of traveling pulses in the 1D model. This may be verified from [6] by substituting the scalings $\hat{\xi} = \sqrt{B/D}\xi$, $\hat{V} = (U_0/B)V$, and $U = U_0\hat{U}$ into Eq. (3.3) there. Moreover, the higher order term there, $-c\sqrt{D/B}\hat{u}_{\hat{\xi}}$, can be identified with the higher order term, $(-1/(\hat{\xi} + \sqrt{B/DR}))\hat{u}_{\hat{\xi}}$ here, since $-1/(\hat{\xi} + \sqrt{B/DR}) = -\sqrt{D/B}/(\sqrt{D/B}\hat{\xi} + R) \sim -(1/R)\sqrt{D/B}$, associating c with $1/R$. This identification is expected, because of the well-established relation between curvature of stationary, axisymmetric pulse and front solutions in dimensions $n \geq 2$ and speed of traveling pulses and fronts, respectively, in one space dimension.

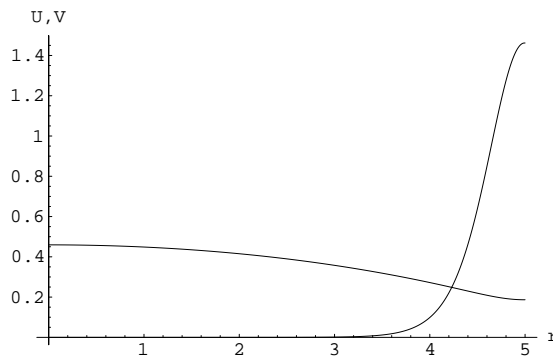


Fig. 5. The asymptotic state of a simulation where $A = 0.08$, $B = 0.2$, $D = 0.01$ and $r_{\max} = 5$. The initial data was of the form (2.39), with $R = r_{\max} = 5$.

Quantitatively, the scalings used here correspond to the scalings in Case Ib of [6,7], which is a regime in which traveling pulses with constant wave speed were found in the 1D Gray–Scott model. We recall from [7] that case I corresponds to $B^{3/2}\sqrt{D}/\sqrt{A} \ll 1$, which holds here. Moreover, in [7] the distinction between subcases a and b is whether $c^2 \ll A$ or $c^2 = \mathcal{O}(A)$, respectively. Translating these using the identification of c with $1/R$, we find either $\sqrt{A}R \gg 1$ or $\sqrt{A}R = \mathcal{O}(1)$, respectively. For the numerical simulations reported in Fig. 4, one has $\sqrt{A}R \approx 0.66$ and 0.49, respectively, in the left and right frames, which are $\mathcal{O}(1)$. Finally, this same identification of $1/R$ with c suggests that it may be possible to find annular ring solutions for which the central radius R is a slowly increasing function of time, since it was shown in [6,7] that in case Ia there exist modulating two-pulse solutions with slowly decreasing wave speed.

3. Destabilization of annular ring solutions into spots

In this section, we examine linear instability properties of the solutions, henceforth denoted by $(U_0(r), V_0(r))$, constructed in the last section. The linearization of the full Gray–Scott problem (1.1) (with $D_U = 1, D_V \equiv D$) about the stationary axisymmetric solution $(U_0(r), V_0(r))$ yields a system of two coupled second-order equations. Returning to the variable $\xi = r - R$ centered on the annular ring \mathcal{A} , we substitute the perturbation:

$$(U(\xi, \theta, t), V(\xi, \theta, t)) = (U_0(\xi), V_0(\xi)) + (u(\xi), v(\xi)) e^{im\theta} e^{\lambda t} \tag{3.1}$$

into (1.1), where m is an integer, and linearize, obtaining

$$\begin{aligned} u_{\xi\xi} + \frac{u_\xi}{\xi + R} &= V_0^2 u + 2U_0 V_0 v + \frac{m^2 u}{(\xi + R)^2} + \lambda u + Au, \\ Dv_{\xi\xi} + \frac{Dv_\xi}{\xi + R} &= -V_0^2 u - 2U_0 V_0 v + \frac{Dm^2 v}{(\xi + R)^2} + \lambda v + Bv. \end{aligned}$$

The structure of this eigenvalue problem is clarified by an appropriate rescaling. The significant scaling of the eigenfunctions u and v is the same as the scaling used on the variables U and V in the existence analysis, and V_0 and ξ are scaled exactly as before. Hence, we set

$$\hat{\xi} = \sqrt{\frac{B}{D}} \xi, \quad \hat{u} = \frac{u}{U_0}, \quad \hat{v} = \frac{U_0}{B} v, \quad \hat{V}_0 = \frac{U_0}{B} V_0, \quad \lambda = B\hat{\lambda}, \quad m = c_1 \hat{m}. \tag{3.2}$$

At this stage of the analysis, c_1 is a free parameter, and the scaling for λ is chosen to simplify the v equation. Since U_0 is given by (2.24) to leading order, the eigenvalue problem is

$$\begin{aligned} \hat{u}_{\hat{\xi}\hat{\xi}} + \frac{\hat{u}_{\hat{\xi}}}{\hat{\xi} + \sqrt{B/DR}} &= \frac{A}{36B^2L^2} \left(\hat{u} \hat{V}_0^2 + 2\hat{V}_0 \hat{v} + 36L^2 B D \hat{u} + \frac{36L^2 B^2 D}{A} \hat{\lambda} \hat{u} + \frac{36B^2 L^2}{A} \frac{c_1^2 \hat{m}^2 \hat{u}}{(\hat{\xi} + \sqrt{B/DR})^2} \right), \\ \hat{v}_{\hat{\xi}\hat{\xi}} + \frac{\hat{v}_{\hat{\xi}}}{\hat{\xi} + \sqrt{B/DR}} &= \left(\frac{c_1^2 \hat{m}^2}{(\hat{\xi} + \sqrt{B/DR})^2} + \hat{\lambda} - 2\hat{V}_0 + 1 \right) \hat{v} - \hat{V}_0^2 \hat{u}. \end{aligned} \tag{3.3}$$

3.1. Transformation of eigenvalue problem to a second-order NLEP

In this section, we reduce the coupled second-order equations (3.3) to a single, second-order, nonlocal eigenvalue problem (NLEP). The procedure for obtaining the NLEP relies on exploiting the fast–slow structure of the underlying annular ring pattern $(U_0(\xi), V_0(\xi))$ to determine the fast–slow structure of the eigenfunctions. One can either encode

asymptotic information about the slow (\hat{u}) component in the fast part of the eigenvalue problem (namely, the \hat{v} equation) or vice versa. We choose the former.

Consider first the slow (outer) \hat{u} problem in the slow variable ξ . Outside an $\mathcal{O}(\sqrt{D/B})$ neighborhood of $\xi = 0$, \hat{V}_0 is exponentially small. Thus, terms in the \hat{u} equation involving \hat{V}_0 can be neglected to leading order. The solution of the outer problem consists of two pieces: $\hat{u}_{\ell 0}$ is the “left outer” solution for $-R < \xi < 0$ and \hat{u}_{r0} is the “right outer” solution for $0 < \xi < r_{\max} - R$. Both $\hat{u}_{\ell 0}$ and \hat{u}_{r0} are obtained by solving:

$$\hat{u}_{\xi\xi} + \frac{\hat{u}_{\xi}}{\xi + R} = \left(\frac{c_1^2 \hat{m}^2}{(\xi + R)^2} + B\hat{\lambda} + A \right) \hat{u} \quad (3.4)$$

with boundary conditions:

$$\hat{u}_{\xi}|_{\xi=-R} = 0, \quad \hat{u}_{\xi}|_{\xi=r_{\max}-R} = 0, \quad \hat{u}(0) = C,$$

where we recall that $d/d\hat{\xi} = \sqrt{D/B}(d/d\xi)$. The first two boundary conditions are imposed so that the boundary conditions of the full partial differential equation (1.1) are satisfied, while the last boundary condition is a matching condition on the left outer and right outer solutions, with the value of C to be determined by matching. The solutions of (3.4) satisfying the given boundary conditions are

$$\begin{aligned} \hat{u}_{\ell 0}(\xi) &= \frac{C}{I_{c_1 \hat{m}}(\sqrt{A + B\hat{\lambda}R})} I_{c_1 \hat{m}}\left(\sqrt{A + B\hat{\lambda}(\xi + R)}\right), \\ \hat{u}_{r0}(\xi) &= \frac{C}{Q} \left(B_2(r_{\max}) I_{c_1 \hat{m}}\left(\sqrt{A + B\hat{\lambda}(\xi + R)}\right) + B_1(r_{\max}) K_{c_1 \hat{m}}\left(\sqrt{A + B\hat{\lambda}(\xi + R)}\right) \right), \end{aligned} \quad (3.5)$$

where

$$\begin{aligned} B_1(r) &= I_{c_1 \hat{m}-1}\left(\sqrt{A + B\hat{\lambda}r}\right) + I_{c_1 \hat{m}+1}\left(\sqrt{A + B\hat{\lambda}r}\right), \quad B_2(r) = K_{c_1 \hat{m}-1}\left(\sqrt{A + B\hat{\lambda}r}\right) + K_{c_1 \hat{m}+1}\left(\sqrt{A + B\hat{\lambda}r}\right), \\ Q &= B_1(r_{\max}) K_{c_1 \hat{m}}\left(\sqrt{A + B\hat{\lambda}R}\right) + B_2(r_{\max}) I_{c_1 \hat{m}}\left(\sqrt{A + B\hat{\lambda}R}\right). \end{aligned}$$

Here, $I_{c_1 \hat{m}}$ and $K_{c_1 \hat{m}}$ are the modified Bessel functions, and we recall that K diverges as its argument vanishes.

As we just saw, (3.4) consists of two separate and fully determined boundary value problems, one problem on the disk $\xi \in [-R, 0)$, and the other on the annulus $\xi \in (0, r_{\max} - R]$, with a continuity condition in \hat{u} at $\xi = 0$. Thus, both problems have two boundary conditions, and there is in general a jump discontinuity in the derivative of \hat{u} at $\xi = 0$, which we label $\Delta_s \hat{u}_{\xi}$. Using (3.5), we find

$$\Delta_s \hat{u}_{\xi} = \lim_{\xi \rightarrow 0^+} \hat{u}_{\xi} - \lim_{\xi \rightarrow 0^-} \hat{u}_{\xi} = -C \sqrt{A + B\hat{\lambda}\Omega},$$

where

$$\Omega = \frac{B_1(r_{\max})}{2Q} \left[B_1(R) \frac{K_{c_1 \hat{m}}(\sqrt{A + B\hat{\lambda}R})}{I_{c_1 \hat{m}}(\sqrt{A + B\hat{\lambda}R})} + B_2(R) \right]. \quad (3.6)$$

We will match the jump discontinuity just computed in the slow field with that computed below in the fast/inner field to determine the value of C . Hence, we rewrite the jump $\Delta_s \hat{u}_{\xi}$ in terms of the fast variable $\hat{\xi}$:

$$\Delta_s \hat{u}_{\hat{\xi}} = -C \sqrt{\frac{AD}{B} + D\hat{\lambda}\Omega}. \quad (3.7)$$

We next consider the leading order \hat{u} problem in the fast regime given by first part of (3.3). By the scaling assumption (2.6), we may neglect to leading order the term involving $\hat{u}_{\hat{\xi}}$. In addition, we binomially expand the term involving \hat{m} , set $c_1 = \sqrt{BR}$, and recall (2.24) to obtain

$$\hat{u}_{\hat{\xi}\hat{\xi}} = \frac{BD}{U_0^2}(\hat{V}_0^2\hat{u} + 2\hat{V}_0\hat{v}) + D(\hat{\lambda} + \hat{m}^2)\hat{u}. \tag{3.8}$$

Recalling the assumptions $D \ll 1$ and $BD/U_0^2 \ll 1$ (2.11), the \hat{u} component of the eigenfunction is constant to leading order in the fast regime. We will focus our attention on the regime in which

$$D \ll \frac{BD}{U_0^2} \Rightarrow \frac{B}{U_0^2} \gg 1,$$

so that the second term on the right-hand side of (3.8) can be neglected. Note that with (2.11) and (2.24) this implies that

$$D \ll \frac{A}{36B^2L^2} \ll 1.$$

(We emphasize that by our choice of scalings we are only studying $\hat{m} = \mathcal{O}(1)$ here. For larger values of \hat{m} one needs to include the second term.) The jump in the derivative of \hat{u} at $\hat{\xi} = 0$, $\Delta_f \hat{u}_{\hat{\xi}}$, is given to leading order by

$$\Delta_f \hat{u}_{\hat{\xi}} = \frac{BD}{U_0^2} \int_{-\infty}^{\infty} (\hat{V}_0^2\hat{u} + 2\hat{V}_0\hat{v}) d\hat{\xi}, \tag{3.9}$$

where we have once again used the fact that \hat{V}_0 decays exponentially outside an $\mathcal{O}(1)$ neighborhood of $\hat{\xi} = 0$. Also, the tails $\int_{-\infty}^{-k} (\hat{V}_0^2\hat{u} + 2\hat{V}_0\hat{v}) d\hat{\xi}$ and $\int_k^{\infty} (\hat{V}_0^2\hat{u} + 2\hat{V}_0\hat{v}) d\hat{\xi}$, where $2k$ is the width of the fast field, introduce an exponentially small error.

Matching requires that one equates $\Delta_s \hat{u}_{\hat{\xi}}$ (3.7) and $\Delta_f \hat{u}_{\hat{\xi}}$ (3.9):

$$-C\sqrt{\frac{AD}{B} + D\hat{\lambda}\Omega} = \frac{BD}{U_0^2} \left[C \int_{-\infty}^{\infty} \hat{V}_0^2 d\hat{\xi} + 2 \int_{-\infty}^{\infty} \hat{V}_0\hat{v} d\hat{\xi} \right].$$

Solving for C and substituting in the leading order value (2.24) for U_0 , one obtains

$$C = \frac{-2}{d(6L)^2\sqrt{A/B + \hat{\lambda}\Omega} + 6} \int_{-\infty}^{\infty} \hat{V}_0\hat{v} d\hat{\xi}, \tag{3.10}$$

where $d = B^2\sqrt{D}/A$. Therefore, one obtains the second-order NLEP:

$$\hat{v}_{\hat{\xi}\hat{\xi}} + [2\hat{V}_0 - (1 + D\hat{m}^2 + \hat{\lambda})]\hat{v} = -C\hat{V}_0^2,$$

by substituting (3.10) for \hat{u} in the \hat{v} equation of (3.3) and neglecting the term involving $\hat{v}_{\hat{\xi}}$, since it is of higher order. Finally, transforming this equation via

$$P^2 = 4(1 + D\hat{m}^2 + \hat{\lambda}), \quad \bar{C} = \frac{-27C}{\int_{-\infty}^{\infty} \hat{V}_0\hat{v} d\hat{\xi}} = \frac{9}{d6L^2\sqrt{\frac{A}{B} + \hat{\lambda}\Omega} + 1}, \quad t = \frac{\hat{\xi}}{2}, \quad y(t) = \hat{v}(\hat{\xi}) \tag{3.11}$$

and using (2.9), one obtains the NLEP:

$$\ddot{y} + (12 \operatorname{sech}^2(t) - P^2)y = \bar{C} \operatorname{sech}^4(t) \int_{-\infty}^{\infty} \operatorname{sech}^2(t)y(t) dt. \tag{3.12}$$

3.2. Analysis of the NLEP

Nontrivial bounded solutions of the NLEP (3.12) for isolated values of P are the leading order fast components of the eigenfunctions of the full eigenvalue problem (3.3). If for a given wave number \hat{m} there exist nontrivial solutions y of (3.12) with $\text{Re}(\hat{\lambda}) > 0$ then $(U_0(\xi), V_0(\xi))$ is linearly unstable to perturbations with (unscaled) wave number $m = \sqrt{BR}\hat{m}$.

For a given solution $y(t)$ of (3.12), the integral in the right member is a constant. Thus (3.12) is equivalent to an inhomogeneous hypergeometric equation:

$$\ddot{y} + (12 \text{sech}^2(t) - P^2)y = \hat{c} \text{sech}^4(t)$$

and classical results from mathematical physics enable us to solve it, see [29], for example. Once one has the solution $\hat{y}(t)$ of this inhomogeneous equation, one has to impose the consistency condition that $\hat{c} = \bar{C} \int_{-\infty}^{\infty} \text{sech}^2(t) \hat{y}(t) dt$. The details of this procedure for solving (3.12) are presented in the appendix. The result of the analysis is an explicit formula $\bar{C} = \bar{C}(P)$, which, for a particular set of parameter values (A, B, D, R, r_{\max}) , relates the angular wave number \hat{m} and the eigenvalue $\hat{\lambda}$:

$$\bar{C}(P) = \frac{P(P-1)(P-2)(P-3)}{16\mathcal{R}(P)}.$$

See Appendix A, where we drop the overbar on $\bar{C}(P)$, for the details of the analysis. This analysis follows [8] closely.

Inverting the formula for \bar{C} (A.12), we obtain the equation:

$$dL^2 = \frac{1}{6\Omega(\hat{\lambda}, \hat{m})\sqrt{A/B + \hat{\lambda}}} \left(\frac{9}{\bar{C}(2\sqrt{1 + D\hat{m}^2 + \hat{\lambda}})} - 1 \right). \quad (3.13)$$

In order to solve (3.13), we develop another Mathematica code [47]. The steps in obtaining the solutions are as follows. Using the parameters (A, B, D, r_{\max}) , we numerically solve (2.36) for R . With the values of (A, B, D, r_{\max}, R) fixed, and where we also recall (2.21), (3.13) depends only on \hat{m} and $\hat{\lambda}$. We loop through a mesh of \hat{m} values and, using the secant method built in to Mathematica, we solve for $\hat{\lambda}$. The result is a list of wave number–eigenvalue pairs $(\hat{m}, \hat{\lambda})$. Finally, we unscale the list, obtaining the $(m, \text{Re}(\lambda))$ pairs, which we plot (see Figs. 6 and 7).

3.3. Numerical simulations: rings splitting into spots

In this section, we compare the results of simulations of the full Gray–Scott problem with the analytic instability results obtained in the previous section. We use the VLUGR2 code [1] to simulate the full 2D problem. This Fortran 77 code uses an adaptive mesh with locally uniform grid refinement to resolve large spatial-temporal gradients.

We simulated the full Gray–Scott problem in polar coordinates (r, θ) . Neumann boundary conditions were used. The initial data were either of the axisymmetric form:

$$U = \alpha - \beta \text{sech}^2\left(\frac{R-r}{\varepsilon_U}\right), \quad V = \gamma \text{sech}^2\left(\frac{R-r}{\varepsilon_V}\right) \quad (3.14)$$

or of the form:

$$U = \alpha - \beta \text{sech}^2\left(\frac{R-r}{\varepsilon_U}\right) \cos^2\left(\frac{n}{2}\theta\right), \quad V = \gamma \text{sech}^2\left(\frac{R-r}{\varepsilon_V}\right) \cos^2\left(\frac{n}{2}\theta\right), \quad (3.15)$$

where for most simulations we took $\alpha = 1.0$, $\beta = 0.6$, $\gamma = 1.4$. Both ε_U and ε_V were chosen to make a large-amplitude pulse in the domain, localized about $r = R$. Initial data of the form (3.14) is as described above,

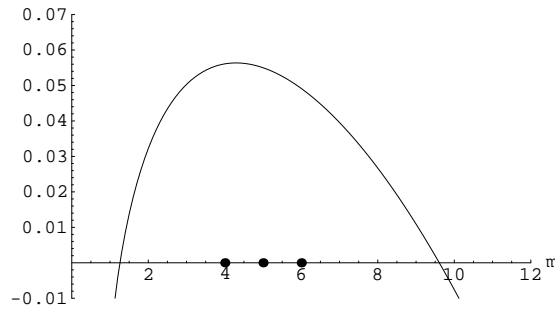


Fig. 6. Prototypical simulation 1: comparison with the stability analysis for $A = 0.04$, $B = 0.102$, $D = 0.01$ and $R = 3.01$. The vertical axis is $\text{Re}(\lambda)$, while the horizontal axis is the (unscaled) wave number m . The black dots at $m = 4$ – 6 correspond to the wave numbers of the stable m -spot patterns that were observed in the numerical simulations. The curve is the plot of $\text{Re}(\lambda)$ of the most unstable eigenvalue obtained from the analysis, and its local maximum is near 4, with $m = 3$ and 5 also being strongly unstable wave numbers.

while the initial data of the form (3.15) consists of a ring of n spots. R was chosen appropriately for each simulation, as explained below. The r -domain was typically taken to be $[0, 5]$, i.e., $r_{\max} = 5$.

The simulations were carried out as follows. For most of the simulations, we chose $D_U = 1$, while $D_V = 0.01$, so that $D \equiv (D_V/D_U) = 0.01$. For fixed values of A , B , D , and r_{\max} , we solved (2.36) numerically to obtain an approximation of R . All simulations were run until the timesteps taken were of the maximum allowable size by the code.

Prototypical simulation 1. $A = 0.04$, $B = 0.102$, $D = 0.01$, $r_{\max} = 5$, $\sqrt{d}L \approx 0.21$, $L \approx 1.28$ (Fig. 6)

Using the above values for the parameters, we find by solving (2.36) numerically that $R \approx 3.01$. The above values for the parameters along with this estimated value of R fix the left-hand side of (3.13). Using the code described at the end of the previous section, we obtain the wave number—eigenvalue list $(m, \text{Re}(\lambda))$ of the most unstable eigenvalue. For the simulations of the full Gray–Scott problem, initial data consisting of a ring of n spots was used. We found that four-, five- and six-spot initial data evolved to stable four-, five- and six-spot patterns, respectively. For initial data consisting of fewer than four spots or more than six spots, the final asymptotic pattern was a four-, five- or six-spot pattern (see Fig. 6).

Prototypical simulation 2. $A = 0.08$, $B = 0.2$, $D = 0.01$, $r_{\max} = 5$, $\sqrt{d}L \approx 0.22$, $L \approx 0.98$ (Figs. 7 and 8).

Using the above values for the parameters, we find from (2.36) that $R \approx 3.13$. The above values for the parameters along with the estimated value of R fix the left-hand side of (3.13). Running the code as described above, we obtain the

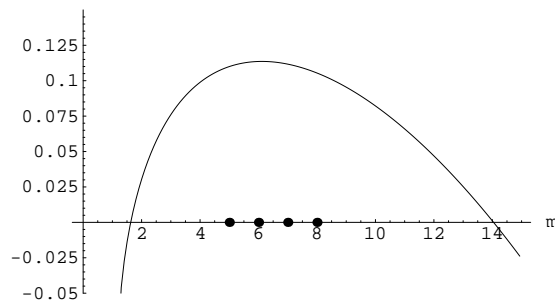


Fig. 7. Prototypical simulation 2: comparison with the stability analysis for $A = 0.08$, $B = 0.2$, $D = 0.01$, $\sqrt{d}L \approx 0.22$, $L \approx 0.98$, and $R = 3.13$. The vertical axis is $\text{Re}(\lambda)$, while the horizontal axis is the (unscaled) wave number m . The black dots at $m = 5$ – 8 correspond to the wave numbers of the stable m -spot patterns that were observed in the numerical simulations. The curve is the plot of $\text{Re}(\lambda)$ of the most unstable eigenvalue obtained from the analysis, and the local maximum is near $m = 6$, with $m = 5$ and 7 also being strongly unstable wave numbers.

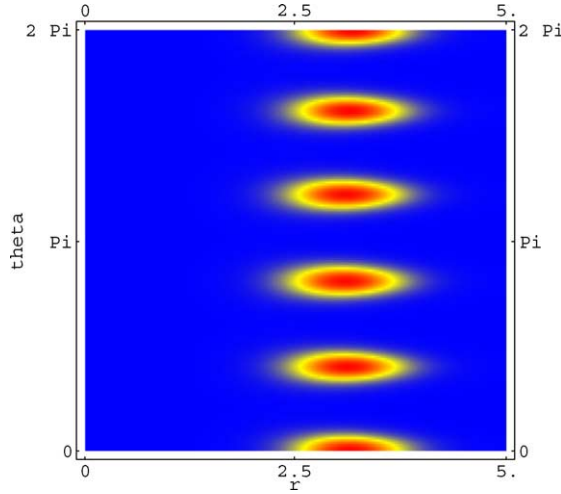


Fig. 8. Prototypical simulation 2 with $A = 0.08$, $B = 0.2$, $D = 0.01$, $R \approx 3.13$ and $T_{\text{end}} = 5000$. The domain is $(r, \theta) = [0, 5] \times [0, 2\pi]$, and initial data are as described in the first paragraphs of Section 3.3. The value of U at the center of the spots is approximately 0.08.

wave number–eigenvalue list $(m, \text{Re}(\lambda))$ of the most unstable eigenvalue. For the simulations of the full Gray–Scott problem, initial data consisting of a ring of n spots was used. We found that four- through eight-spot initial data evolved to stable four- to eight-spot patterns, respectively. For initial data consisting of fewer than four spots or more than eight spots, the final asymptotic pattern had between four and eight spots positioned on a ring (see Figs. 7 and 8).

3.4. Comparison of theory and simulations; stable ring solutions on long time scales

In this section, we compare the results of a series of simulations with the leading order NLEP theory, where this series is chosen to examine the effects of increasing the small parameter $A/36B^2L^2$. Specifically, we fix the domain size and parameters A and D , and choose a decreasing sequence of values B . For each set of parameters, we determine via the NLEP the wave numbers to which the annular ring solution is unstable, and hence the number of spots the ring splits into. These predictions are then checked against direct numerical simulations for different sets of initial data (3.15), where R is calculated from the leading order theory of Section 2 and n is an integer chosen from the set $\{3, 4, \dots, 13, 14\}$. We recall that the stability analysis is for long, but not infinite, time scales.

Specifically, we fixed the domain size to be $r_{\text{max}} = 5$, and $A = 0.04$, while $D = 0.005$ is chosen small enough so that we could obtain reasonable comparisons with the leading order theory, but large enough so that the problem could be computed. B was chosen from the following set of decreasing values $\{0.14, 0.12, 0.1, 0.08, 0.06, 0.05, 0.045, 0.04, 0.038\}$. The results are given in Table 2. Just as was the case for the prototypical simulations presented above, it is the case for the series of simulations reported here that the most unstable wave numbers calculated with the NLEP method quantitatively correspond to the number of spots observed in the PDE (1.1). Moreover, as the value of the small parameter $A/36B^2L^2$ was increased, the width of the interval of unstable wave numbers decreased, until it vanished near 0.22. We found similar results for other values of D .

For completeness, we note [39] that the m value at the left edge of the instability interval can be computed directly from condition (3.13), since there the real part of $\hat{\lambda}$ vanishes, simplifying the condition. See the analysis of homoclinic stripes and their splitting into spots in [13], where this idea was first used.

Table 2

The number of spot solutions predicted by the NLEP, and the actual number of spot solutions which are stable to $T_{\text{end}} = 1000$, as given by the results of simulations^a

B	$A/36B^2L^2$	NLEP prediction (no. of spots)	Most unstable wave numbers	Simulations
0.14	0.036	2–16	5–7	4–8
0.12	0.046	2–15	5–7	4–9
0.1	0.062	2–14	5–7	5–9
0.08	0.091	3–12	5–7	5–9
0.06	0.15	4–9	5–7	5–8
0.05	0.22	Stable ring	–	6–7
0.04	0.33	Stable ring	–	Stable ring

^a Shown also is the value of the small parameter, $A/36B^2L^2$, which increases as B decreases. In each case, the NLEP curve attains its maximum at $m = 6$, with the most unstable interval of wave numbers being 5–7 in each case. Note that for $B = 0.05$, the NLEP prediction has a maximum of about -0.002 near $m = 6$, and it is expected that higher order corrections would move the NLEP curve above the m -axis. Finally, on significantly longer time scales, some spotted ring solutions undergo secondary instabilities.

4. Turing/Ginzburg–Landau analysis

The analysis in the previous sections has been for the monostable regime ($A < 4B^2$), in which ($U = 1, V = 0$) is the only homogeneous stable state. In this section, we focus on the bistable regime ($A > 4B^2$). The two additional homogeneous steady states are

$$(U_{\pm}, V_{\pm}) = \left(\frac{1}{2} \left[1 \pm \sqrt{1 - \frac{4B^2}{A}} \right], \frac{A}{2B} \left[1 \mp \sqrt{1 - \frac{4B^2}{A}} \right] \right). \quad (4.1)$$

The state (U_-, V_-) is conditionally stable, see [27], and we perform a linearized stability analysis of it, also verifying the results via numerical simulation. In addition, we show numerically that some of the annular ring solutions studied in the monostable regime may be continued into this bistable regime.

4.1. Stability with respect to radial and angular perturbations

We consider perturbations of the form:

$$\begin{pmatrix} U \\ V \end{pmatrix} = \begin{pmatrix} U_- \\ V_- \end{pmatrix} + \begin{pmatrix} u(t) \\ v(t) \end{pmatrix} f(k, m, r, \theta), \quad (4.2)$$

where $f(k, m, r, \theta)$ is taken from the set $\{J_0(kr), J_0(kr) e^{im\theta}, e^{im\theta}\}$, where $J_0(kr)$ is the Bessel function of the first kind. First, substituting (4.2) with $f = J_0(kr)$ into (1.1) and linearizing, one obtains

$$\begin{pmatrix} \dot{u} \\ \dot{v} \end{pmatrix} = \mathcal{M} \begin{pmatrix} u \\ v \end{pmatrix}, \quad (4.3)$$

where

$$\mathcal{M} \equiv \begin{pmatrix} -k^2 - \frac{A^2}{B^2} - A & -2B \\ \frac{A^2}{B^2} & B - Dk^2 \end{pmatrix}. \quad (4.4)$$

Here, we used the leading order approximation:

$$(U_-, V_-) = \left(\frac{B^2}{A}, \frac{A}{B} \right) \quad (4.5)$$

for U_- and V_- , since $4B^2 < A$. In addition, since the derivatives of $J_0(z)$ involve $J_1(z)$ and $J_{-1}(z)$, the recurrence relation:

$$J_{\nu-1}(z) - \frac{2\nu}{z}J_\nu(z) + J_{\nu+1}(z) = 0$$

was used to write the $J_{\pm 1}(z)$ in terms of $J_0(z)$.

The more general perturbation:

$$\begin{pmatrix} U \\ V \end{pmatrix} = \begin{pmatrix} U_- \\ V_- \end{pmatrix} + \begin{pmatrix} u(t) \\ v(t) \end{pmatrix} J_m(kr) e^{im\theta}, \quad (4.6)$$

leads to the same stability matrix \mathcal{M} , as given by (4.4) above. However, (4.6) is not a complete set of basis functions, since when k is 0, $J_m(0) \equiv 0$, and thus purely angular perturbations are not yet taken into account. We return to this shortly.

Using the trace-determinant form of the eigenvalues of \mathcal{M} :

$$\lambda_{\pm} = \frac{1}{2}[\text{Tr } \mathcal{M} \pm \sqrt{(\text{Tr } \mathcal{M})^2 - 4 \text{Det } \mathcal{M}}],$$

we see that $\text{Re}(\lambda_+) > \text{Re}(\lambda_-)$.

In order for (U_-, V_-) to be linearly stable, it must be that $\text{Tr } \mathcal{M} = \lambda_+ + \lambda_- < 0$ for all k . The trace of \mathcal{M} is

$$-\frac{A^2}{B^2} - A + B - Dk^2 - k^2.$$

Setting $k = 0$ and solving for $A = 0$, one finds that $\text{Tr } \mathcal{M} < 0$ when

$$A < B_- \quad \text{or} \quad A > B_+,$$

where

$$B_{\pm} = \frac{1}{2}B^{3/2}(-\sqrt{B} \pm \sqrt{B+4}).$$

We now find explicit values, A_c and k_c , of the parameter A and wave number k such that (U_-, V_-) is marginally stable. Marginal stability at k_c is equivalent to the situation in which $\text{Re}(\lambda_-) < 0$ for all k and $\text{Re}(\lambda_+) < 0$ for all $k \neq \pm k_c$, $\text{Re}(\lambda_+)|_{k=\pm k_c} = 0$ and $(d/dk)\text{Re}(\lambda_+)|_{k=\pm k_c} = 0$. Since $\text{Det } \mathcal{M} = \lambda_- \cdot \lambda_+$, marginal stability thus occurs for A_c and k_c satisfying

1. $\text{Det } \mathcal{M}(k; A_c) \geq 0$ for all k .
2. $\text{Det } \mathcal{M}(\pm k_c; A_c) = 0$.
3. $(\partial/\partial k)\text{Det } \mathcal{M}(\pm k_c, A_c) = 0$.

Condition 3 implies that locally (near $\pm k_c$) the eigenvalue curve λ_+ meets the k -axis in a quadratic tangency.

From conditions 2 and 3, one obtains

$$A_{\pm} = \frac{B^3 - B^2 D k^2 \pm B \sqrt{B^4 + 4B^2 k^2 - 2B^3 D k^2 + B^2 D^2 k^4 - 4D^2 k^6}}{2(B + D k^2)} \quad (4.7)$$

and

$$A_{\pm} = \frac{-B^2\sqrt{D} \pm B\sqrt{4B + B^2D - 8Dk^2}}{2\sqrt{D}}, \quad (4.8)$$

respectively. Setting the roots (4.7) and (4.8) corresponding to A_+ equal and solving for k^2 , one obtains four possible solutions, one in each quadrant of the (k, A) parameter plane. The solution in the first quadrant is

$$k_c^2 = \frac{B^{3/2}}{\sqrt{2D}} - \frac{B}{D} + \frac{B\sqrt{BD - 4\sqrt{2BD} + 4}}{\sqrt{2D}}. \quad (4.9)$$

Substituting this solution into the formula (4.8) corresponding to A_+ , one obtains the result for A_c :

$$A_c = -\frac{B^2}{2} + \frac{B\sqrt{-4\sqrt{2D}B^{3/2} + DB^2 - 4\sqrt{2}B\sqrt{BD - 4\sqrt{2BD} + 4} + 12B}}{2\sqrt{D}}. \quad (4.10)$$

To study perturbations of the conditionally stable homogeneous state (U_-, V_-) with respect to the angular variable θ , we substitute

$$\begin{pmatrix} U \\ V \end{pmatrix} = \begin{pmatrix} U_- \\ V_- \end{pmatrix} + \begin{pmatrix} u(t) \\ v(t) \end{pmatrix} e^{im\theta}$$

into (1.1) and linearize. The resulting stability problem is the same as (4.3) with $k = m/r$ and hence, $m_c^2 = k_c^2 r^2$.

Finally, we note that the stationary state (U_-, V_-) is linearly stable for $A > A_c$, while for $A < A_c$ it is linearly unstable. Thus, we would expect the formation of Turing patterns to occur for $A < A_c$ and $|A - A_c| \ll 1$.

4.2. Verification of linear stability analysis via numerical simulation of the full 2D problem

In this section, we verify the stability analysis presented in the previous section. We used the VLUGR2 code [1], discussed in Section 3, for our simulations.

Fig. 9 shows the result of a representative simulation. In this case, $A = 0.07$, $B = 0.086$ and $D = 0.01$, which is well below the critical parameter value $A_c \sim 0.106$. The solution has the appearance of a target pattern, where the rings of the pattern have split into spots. The stripe on the left-hand side of the left figure corresponds to a spot centered at the origin. The other two stripes of spots correspond to annular rings of spots. The measured (angular) wavelengths of the center and right stripe are 0.782 and 0.393, respectively, which closely correspond to the theoretically predicted values of 0.782 and 0.435. Note that all numerically calculated wavelengths are accurate to only within half of a characteristic wavelength, due to the fact that we use Neumann boundary conditions in the θ coordinate instead of periodic boundary conditions.

It is interesting to note that if one writes the “angular” Gray–Scott problem obtained from (1.1) by using the polar form of the Laplacian, but keeping only the θ -dependent term, one obtains a problem in which r appears as a parameter. Using the parameters of Fig. 9 with an r value corresponding to the middle of the center ring, simulations of this problem with periodic initial data of period 0.785, one finds that such a solution is stable. Likewise, for r chosen corresponding to the center of the outermost ring, a resulting solution of wavelength 0.393 is found to be stable. This corresponds nicely with the angular wavelengths of the spots seen in Fig. 9.

In addition, hexagonal patterns are also observed near criticality. The patterns observed consist of spots of low activator concentration in a background of high activator concentration (see Fig. 10). Near criticality, one can derive

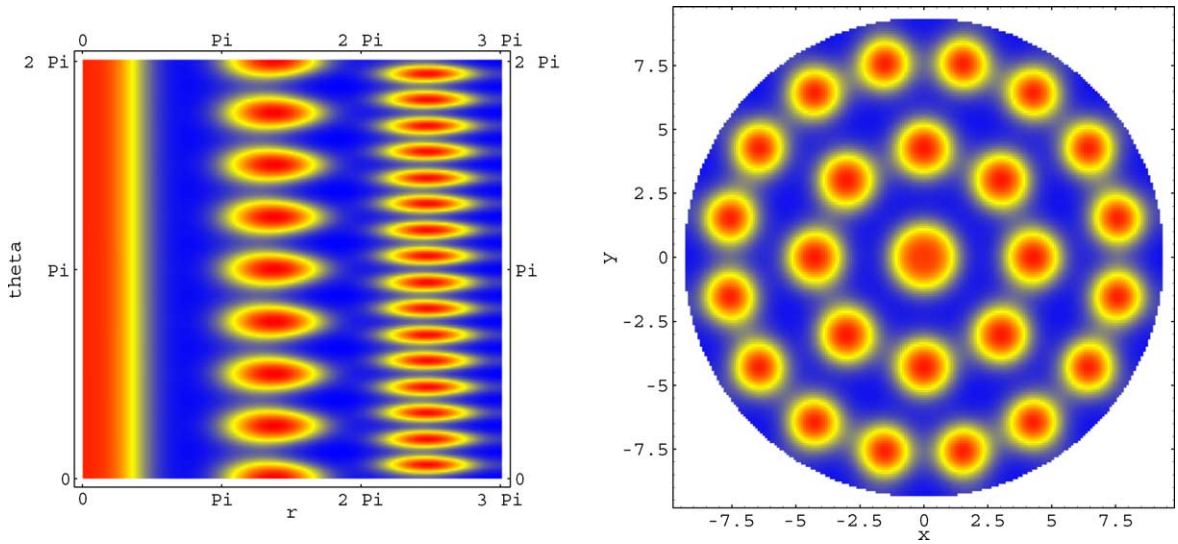


Fig. 9. In this simulation $A = 0.07$, $B = 0.086$, $D = 0.01$, $T_{\text{end}} = 15000$, and the domain size is $(r, \theta) = [0, 3\pi] \times [0, 2\pi]$. The left figure is a plot of simulation data, which is in polar coordinates, while the right figure is obtained by transforming the data of the same simulation into rectangular coordinates. The center ring is located at $r \approx 4.3$ while the outer ring is at $r \approx 7.7$. Initial data were of the form $U = 0.1 + 0.05 \cos(2r)$, $V = 1.1 - 0.6 \cos(2r)$. The destabilization into spots occurs along the ring all at once.

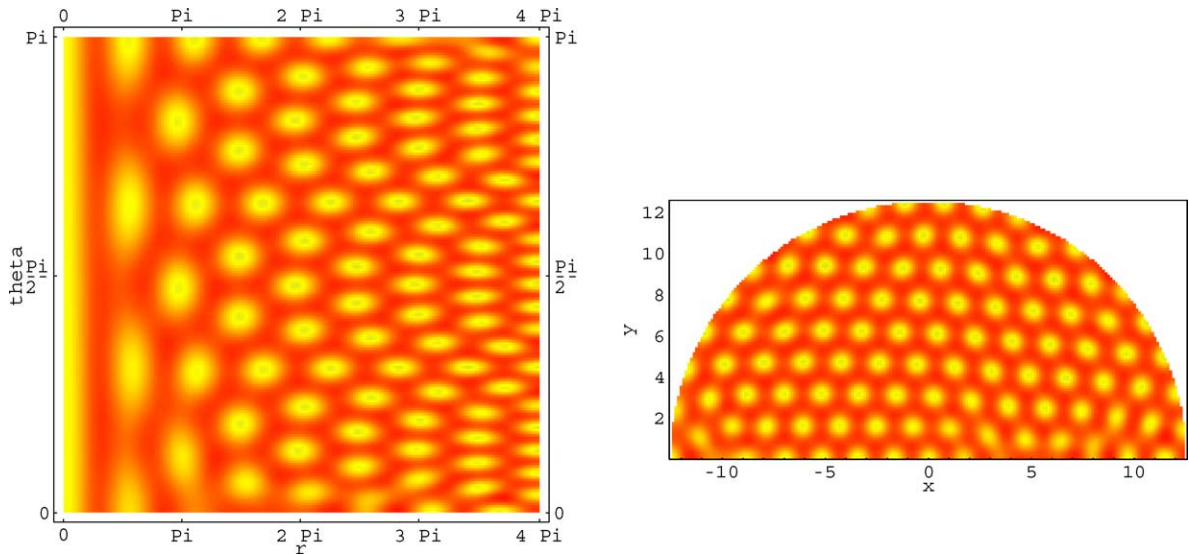


Fig. 10. The left figure shows the activator (V) concentration from a simulation of the full 2D problem in polar coordinates, where the horizontal axis is the r -axis and the vertical axis is the θ -axis, and the right figure shows a plot of the same data in rectangular coordinates. Higher concentrations are denoted by red, while lower concentrations are denoted by yellow. In both plots, $A = 0.1475$, $B = 0.102$ and $D = 0.01$, and the domain is $(r, \theta) = [0, 4\pi] \times [0, \pi]$. The parameters are near critical, with the pattern consisting of small-amplitude displacements from the linearly unstable homogeneous state (U_-, V_-) . The critical value of A calculated from the leading order theory is $A_c \approx 0.137$, and the inclusion of higher order corrections moves A_c above 0.1475. In simulations of the full problem, the target pattern breaks up into spots of low activator concentration against a background of high activator concentration. In the right figure, a hexagonal structure is apparent. The solution is a classic Turing pattern. Initial data was $U = 0.1 + 0.05 \cos(2r)$, $V = 1.3 - 0.6 \cos(2r)$.

amplitude equations to determine the stability of hexagonal patterns. See for example [43, Chapter 14.3], where this is done for the Brusselator.

4.3. Numerical continuation of Turing patterns back to the monostable regime

We next consider simulations of the radially symmetric Gray–Scott equation and show that the Turing patterns just studied in the bistable regime can be continued back into the monostable regime. We fix the parameters A and D and run simulations for a series of values for B . More precisely, we set $A = 0.3$ and $D = 0.001$, and we chose B from the following set:

$$B \in \{0.925, 0.9125, 0.7, 0.5, 0.3, 0.24, 0.15, 0.1, 0.08, 0.07\}.$$

The domain was taken to be $r = [0, 5]$, the homogeneous initial data ($U = U_-, V = V_-$) were used (with a tiny perturbation) and all simulations were run to $T_{\text{end}} = 10^5$. For $B = 0.925$, one obtains the trivial solution $(U, V) = (1, 0)$. For $0.27 < B < 0.925$, one obtains a single pulse solution for V , which corresponds to an annular ring solution of the full problem. As B is decreased below 0.27, multi-pulse solutions begin to appear; first a two-ring solution near $B = 0.26$, then three- and four-ring solutions as B is decreased further.

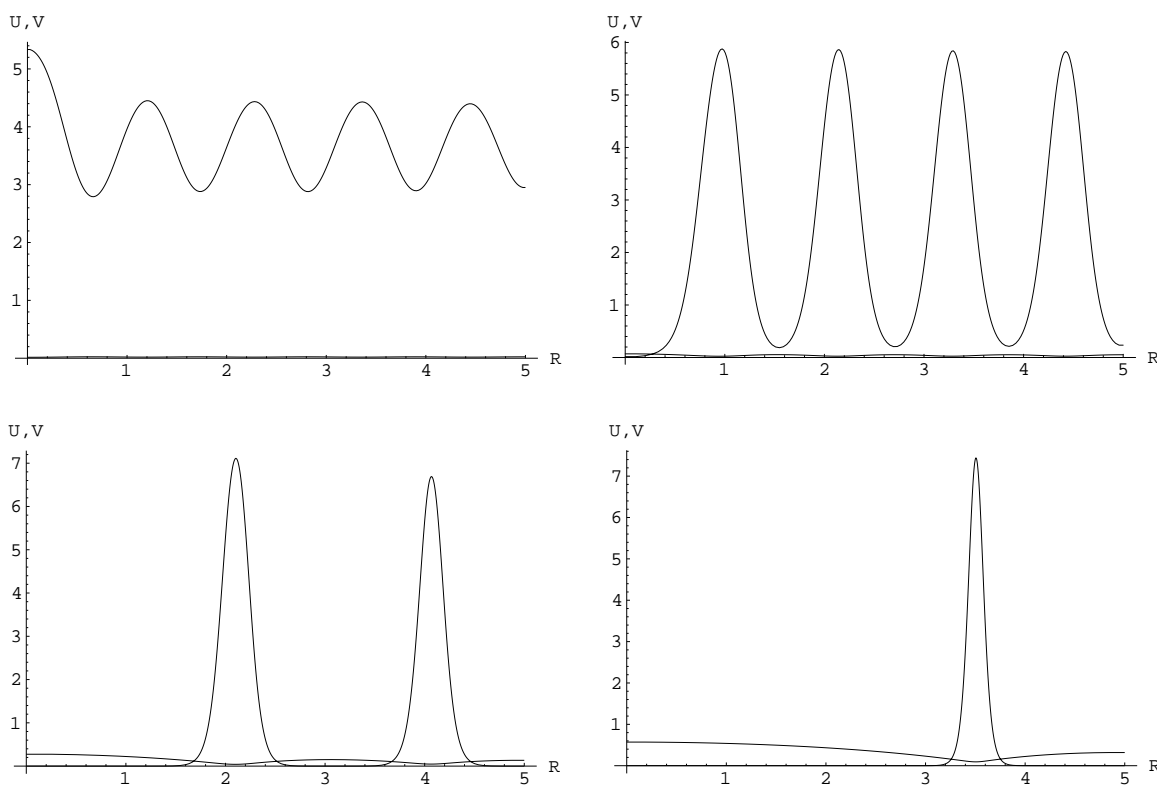


Fig. 11. In the four simulations presented here, $A = 0.3$, $D = 0.001$ and $T_{\text{end}} = 10\,000$. $B = 0.08$ in the top left figure, which is close to the leading order critical $B_c = 0.0804$ (where (U_-, V_-) is marginally stable). The solution lies in the fast field, where V is bounded away from 0. In the top right figure, $B = 0.12$, and the solution is further from critical, and between the rings, V is bounded away from 0. In the lower left figure, $B = 0.24$, which is above B_c . In this regime, (U_-, V_-) still exists and is linearly unstable, and V is now exponentially small between rings. In the lower right figure, $B = 0.5$, and the state (U_-, V_-) no longer exists. This one-ring solution is of the type studied in Section 2.

These multi-pulse solutions resemble the singular solutions discussed in Section 2, in that the solution V has a number of large-amplitude pulses, while away from the pulses, V is exponentially small. However, as B approaches the critical value $B_c = 0.08$ (the value at which (U_-, V_-) is marginally stable), V is no longer exponentially small between pulses. Finally, as B is decreased through B_c , these periodic-like solutions decrease in amplitude to the trivial state (U_-, V_-) (see Fig. 11). This continuation result follows closely the continuation result obtained for spatially periodic patterns in 1D in [27], where Busse balloons (see [3]) of stable states were found.

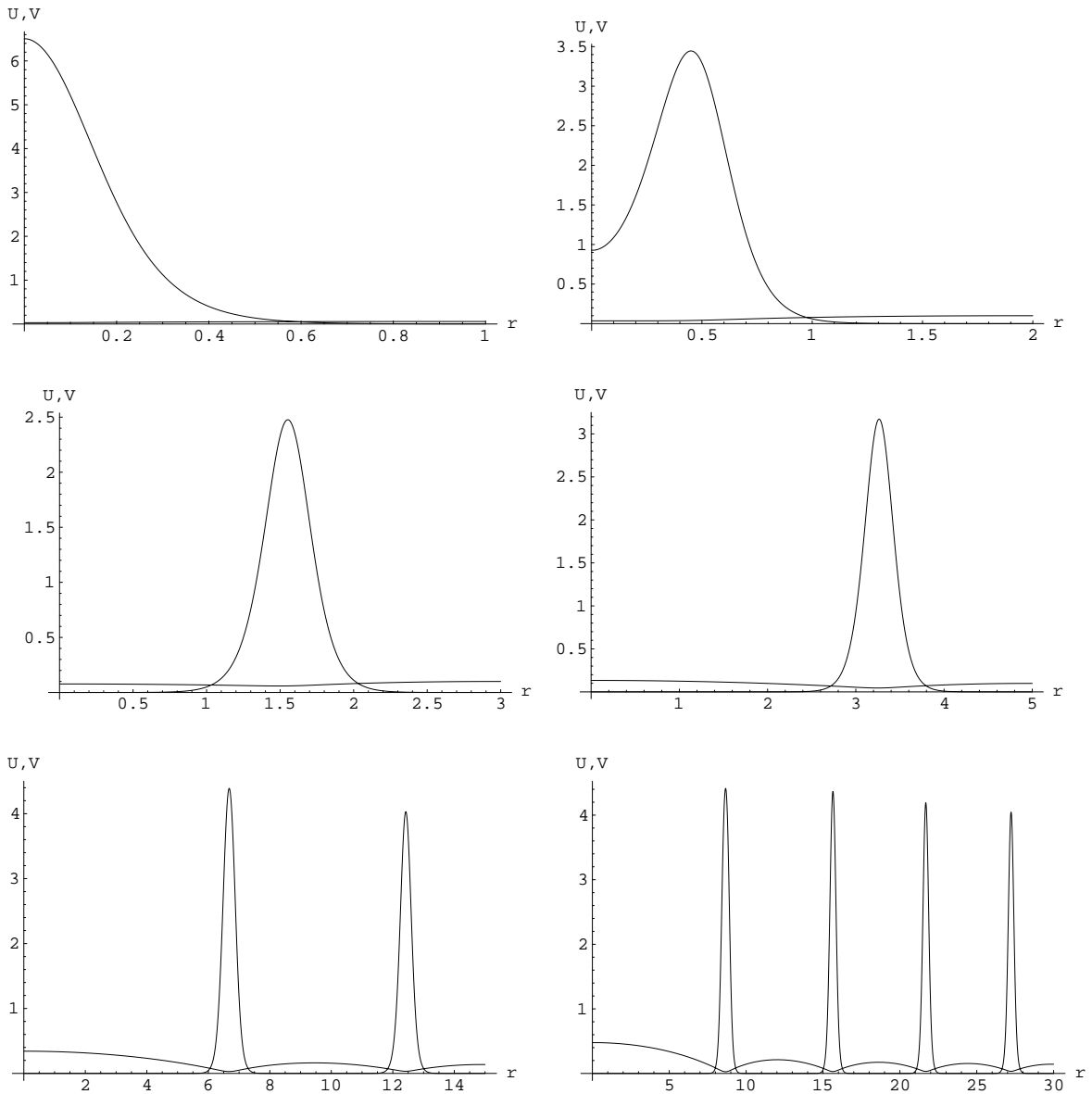


Fig. 12. For the fixed parameters $A = 0.04$, $B = 0.102$, $D = 0.001$, as the disk size is increased, the solution develops from a spot in the center of the domain, to an annular ring, and then to multiple annular rings.

Remark. If one fixes the parameters and instead increases the domain size (that is, increases r_{\max}), the result is that, depending on the magnitude of r_{\max} , an n -ring solution will develop, with n increasing with r_{\max} (see Fig. 12.)

5. Stable stationary ‘volcanos,’ ring splitting and other solutions

In the analysis of Sections 2–4, the existence of axisymmetric annular ring solutions was presented, and linear stability results were obtained for very long, but not infinite, times. We showed that an annular ring solution could break up into a ring of spots and predicted the number of spots from the most unstable angular wave numbers derived from the NLEP method. Interestingly, the widths of the intervals of unstable wave numbers m shrink as the small parameter $A/36B^2L^2$ is increased (recall Table 2). For the simulations reported in Table 2, this interval of instability vanished when the size of the small parameter reached 0.22, and an annular ring solution was observed to exist for long times when the small parameter was near 0.33.

In this final section, we briefly discuss three closely related phenomena. First, we present the results of simulations in the regime where both U and V vary on approximately the same spatial length scale. Here, we find long-lived annular ring solutions. A representative simulation is shown in Fig. 13, where we note that the parameter values are outside the domain in which the above analysis applies. The situation here with annular rings is similar to that for one-pulse solutions in 1D where the existence from the asymptotic regime can be continued into the regime where the concentrations of both species vary over the same spatial length scale, see Section 6 of [8].

In addition, for certain values of the parameters, and starting with annular rings as initial data, the rings were observed to split into two or more rings. As the simulations progress, the outer-most and innermost rings developed a disturbance transverse to the ring. (These zigzag instabilities might be studied along the lines of [19,21].) Continuing the simulations further, we see that the disturbances in the rings propagate into the inner rings. These simulations were run on a rectangular domain, with the boundary far from the rings (Figs. 14 and 15). For the parameter values for which this behavior is observed, U and V vary over (nearly) the same spatial length scale, and so the analytical approach considered in Section 2 of this work might be extended using topological shooting, as was done for pulse solutions in 1D in Section 6 of [8].

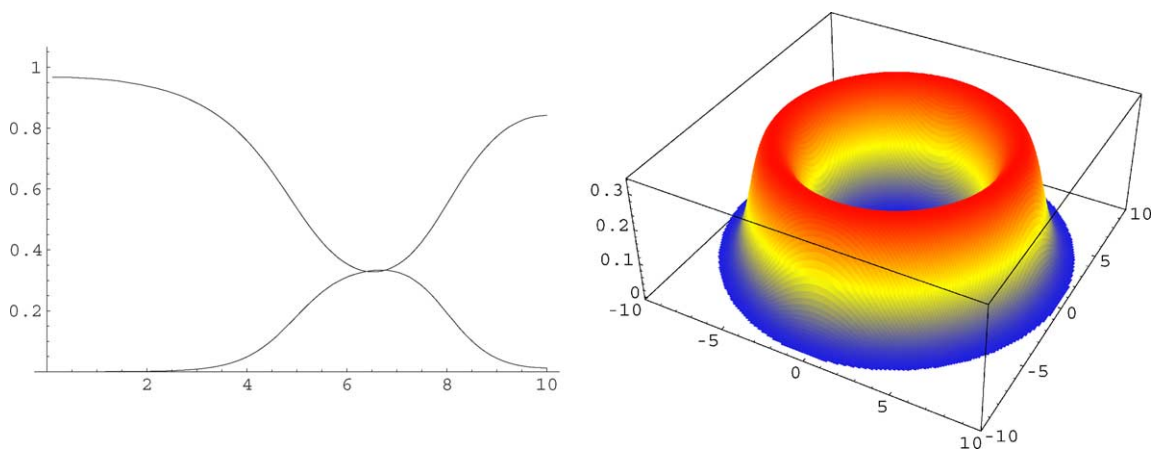


Fig. 13. The results of a simulation in which the parameters were $A = 0.04$, $B = 0.102$, $D_U = 0.05$, $D_V = 0.025$. The domain was the disk $(r, \theta) \in [0, 10] \times [0, 2\pi]$, and the simulation was run to an end time of $T_{\text{end}} = 10,000$. The left figure shows the cross-section of the solution, showing both U and V . Note that U and V vary over roughly the same spatial length scale. The right figure shows the V component of the same solution.

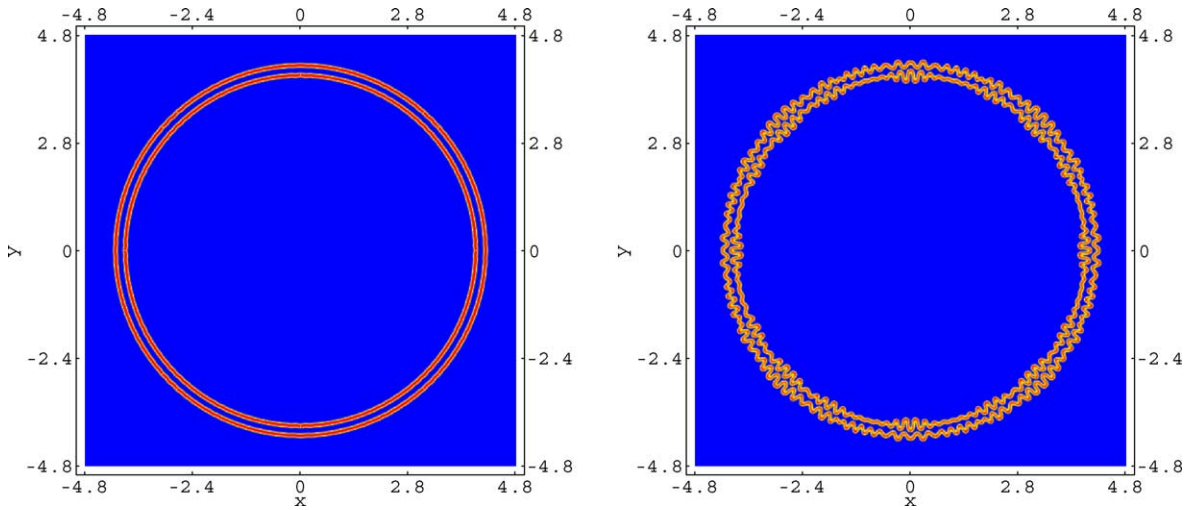


Fig. 14. The V component of simulations for $A = 0.0405$, $B = 0.102$, $D_V = 10^{-5}$, $D_U = 2 \times D_V$. In the left figure, $T_{\text{end}} = 3000$, and one-ring annular initial data has split into two rings. In the right figure, at $T_{\text{end}} = 4000$, the two rings have developed a zig-zag disturbance. See [3,21] for other examples in which zig-zag instabilities arise. Note that these simulations were performed on a rectangular domain $[-10, 10] \times [-10, 10]$, and the above figures do not show the whole domain.

In simulations, isolated spots were also observed to exist. The typical solution consists of an axisymmetric spot solution centered in the middle of the (square) domain. For example, on a square domain of dimension $[-0.15, 0.15] \times [-0.15, 0.15]$, and for $A = 0.01$, $B = 0.145$, $D_U = 0.5625 \times 10^{-3}$, and $D_V = 0.5625 \times 10^{-5}$ such a solitary stationary spot solution is observed. It may be possible to modify the analysis of Section 2 to study their existence, but we do not consider them further here (see [44]).

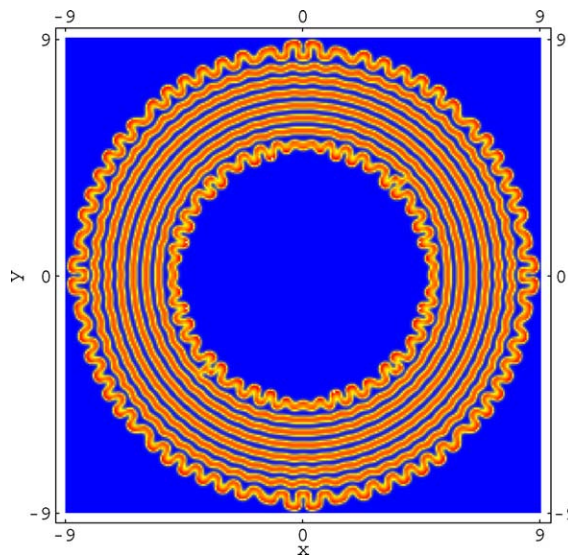


Fig. 15. The V component of simulations for $A = 0.041616$, $B = 0.102$, $D_V = 10^{-5}$, $D_U = 2 \times D_V$, $T_{\text{end}} = 3500$. The domain of the simulation was $[-25, 25] \times [-25, 25]$, and the above figure does not show the full domain. Notice that the outer and inner rings have developed a pronounced zig-zag disturbance.

Acknowledgements

Both authors gratefully acknowledge support from the National Science Foundation via grant DMS-0072596 for the final stages of this work.

Appendix A. Explicit eigenvalue formulae

In this appendix, we make extensive use of the theory of hypergeometric functions to derive an equation for \bar{C} (3.11). We begin with the NLEP (3.12):

$$\ddot{y} + (12 \operatorname{sech}^2(t) - P^2)y = \bar{C} \operatorname{sech}^4(t) \int_{-\infty}^{\infty} \operatorname{sech}^2(t)y(t) dt$$

with the boundary condition that $y : \mathbb{R} \rightarrow \mathbf{C}$ remains bounded as $t \rightarrow \pm\infty$. In this appendix, we drop the overbar on $\bar{C}(P)$.

The unique solution of this nonlocal eigenvalue problem is determined as follows. First, one transforms—in standard fashion (see for instance [29])—the left-hand side into the form of a hypergeometric differential equation by setting $y(t) = F(t)(\operatorname{sech} t)^P$ and then changing independent variables to $x \equiv (1/2)(1 - \tanh t)$:

$$\begin{aligned} x(1-x)F'' + (1+P)(1-2x)F' + (12-P-P^2)F \\ = 2C(4x(1-x))^{1-P/2} \int_0^1 (4x(1-x))^{P/2} F(x) dx. \end{aligned} \quad (\text{A.1})$$

Second, one finds the unique solution $F_{\tilde{C}}$ of the auxiliary (standard, inhomogeneous) problem:

$$x(1-x)F_{\tilde{C}}'' + (1+P)(1-2x)F_{\tilde{C}}' + (12-P-P^2)F_{\tilde{C}} = \tilde{C}(4x(1-x))^{1-P/2}, \quad (\text{A.2})$$

where \tilde{C} is a constant. Recall that $F(a, b|c|z)$ and $z^{1-c}F(b-c+1, a-c+1|2-c|z)$ are two linearly independent solutions of the hypergeometric differential equation:

$$z(1-z)F'' + [c - (a+b+1)z]F' - abF = 0.$$

From (A.2), one sees directly that $a = P+4$, $b = P-3$, and $c = P+1$ (where a and b are interchangeable), and hence the two homogeneous solutions are

$$X(x) = F(P+4, P-3|P+1|x), \quad (\text{A.3})$$

$$Y(x) = \frac{L(P)}{x^P} F(-3, 4|1-P|x), \quad (\text{A.4})$$

where

$$L(P) \equiv \frac{(P-3)(P-2)(P-1)}{(P+3)(P+2)(P+1)}.$$

By the introduction of this additional constant we have $X(1-x) = Y(x)$ (which will be used frequently below). By solving the (standard) differential equation for the Wronskian $W(x)$, we find

$$W(x) \equiv XY' - YX' = \frac{w(P)}{(4x(1-x))^{1+P}}, \quad (\text{A.5})$$

where $w(P) = -4^{1+P}PL(P)$. Moreover, we note that $X(x)$ is analytic at $x = 0$, and that $F(-3, 4|1 - P|x)$ is a cubic polynomial. Now, the solution of the inhomogeneous problem is obtained via variation of constants; i.e., by setting $F_{\tilde{C}}(x) = f(x)X(x) + g(x)Y(x)$. Using (A.5), we find

$$f' = \frac{4^{1-P/2}\tilde{C}}{P(P-1)(P-2)(P-3)}(1-x)^{1+P/2}x^{1-P/2}k(P, x), \quad (\text{A.6})$$

$$g' = -\frac{4^{1-P/2}\tilde{C}}{P(P-1)(P-2)(P-3)}x^{1+P/2}(1-x)^{1-P/2}k(P, 1-x), \quad (\text{A.7})$$

where the cubic polynomial $k(P, \xi) \equiv k_0(P) + k_1(P)\xi + k_2(P)\xi^2 + k_3(P)\xi^3$ with $k_0(P) = (P-3)(P-2)(P-1)$, $k_1(P) = 12(P-3)(P-2)$, $k_2(P) = 60(P-3)$, and $k_3(P) = 120$ can be obtained from $F(-3, 4|1 - P|x)$, and we note that the value of $k_3(P)$ is a correction to a typographical error in [8], but that the other calculations presented there are correct. Therefore, defining

$$\mathcal{F}(x_1, x_2, P) = \int_{x_1}^{x_2} (1-\xi)^{1+P/2}\xi^{1-P/2}k(P, \xi) d\xi, \quad (\text{A.8})$$

the general solution of the inhomogeneous equation (A.1) is

$$F_{\tilde{C}}(x; P) = [d(P)\mathcal{F}(0, x; P) + f_0]Y(1-x; P) + [-d(P)\mathcal{F}(1-x, 1; P) + g_0]Y(x; P), \quad (\text{A.9})$$

where $d(P) \equiv 4^{1-P/2}\tilde{C}/P(P-1)(P-2)(P-3)$ (and of course \tilde{C} is a function of P) and f_0 and g_0 are constants determined by boundary conditions. Specifically, requiring that $F_{\tilde{C}}$ stay bounded as $x \rightarrow 0$ and as $x \rightarrow 1$ implies $g_0 = 0$ (since $Y(x) \rightarrow \infty$ as $x \rightarrow 0^+$ and $\mathcal{F}(1, 1; P) = 0$), while $f_0 = -d(P)\mathcal{F}(0, 1; P)$ (since $Y(1-x) \rightarrow \infty$ as $x \rightarrow 1^-$ and $\mathcal{F}(0, 1; P) \neq 0$). We also observe that $F_{\tilde{C}}(1-x; P) = F_{\tilde{C}}(x; P)$; and, for completeness, we record that

$$\mathcal{F}(0, 1; P) = -\frac{1}{24}P^2 \left(1 + \frac{1}{2}P\right)^2 \left(1 - \frac{1}{2}P\right)^2 \frac{\pi}{\sin((\pi/2)P)}.$$

Third, in order that the solution $F_{\tilde{C}}(x; P)$ given by (A.9) of the auxiliary problem solves the full nonlocal problem (A.1), one requires that $F_{\tilde{C}}$ satisfies the consistency condition:

$$\tilde{C} = 2C \int_0^1 F_{\tilde{C}}(x; P)(4x(1-x))^{P/2} dx. \quad (\text{A.10})$$

Of course, due to the linearity of the auxiliary equation, its unique solution is of the form $F_{\tilde{C}}(x; P) = \tilde{C}F_1(x; P)$. Hence, for nonzero \tilde{C} , the consistency condition (A.10) simplifies to

$$1 = 2C \int_0^1 F_1(x; P)(4x(1-x))^{P/2} dx. \quad (\text{A.11})$$

Finally, inserting the solution (A.9) into the relation (A.11), we obtain

$$C(P) = \frac{P(P-1)(P-2)(P-3)}{16\mathcal{R}(P)}, \quad (\text{A.12})$$

where

$$\mathcal{R}(P) = -\int_0^1 \mathcal{F}(x, 1; P)Y(1-x; P)x^{P/2}(1-x)^{P/2} dx. \quad (\text{A.13})$$

We remark that a straightforward expansion yields

$$\lim_{P \rightarrow 2} C(P) = \frac{9}{2}. \quad (\text{A.14})$$

Finally, the explicit expression (A.12) for $C = C(P)$ is substituted into the explicit expression for dL^2 , which is readily obtained by inverting the second part of (3.11):

$$dL^2 = \frac{1}{6\Omega(\hat{\lambda}, \hat{m})\sqrt{A/B + \hat{\lambda}}} \left[\frac{9}{C(P)} - 1 \right]. \quad (\text{A.15})$$

This relation between dL^2 and P , and thus also the relation between dL^2 and $\hat{\lambda}$, determines the leading order part of the (discrete) eigenvalues of the NLEP. Using the explicit expressions (A.8), (A.12) and (A.13) one can explicitly solve (A.15). However, it is clear that this cannot be done by hand (especially not for complex values of P); one uses a package such as Mathematica [47].

References

- [1] J.G. Blom, R.A. Trompert, J.G. Verwer, Algorithm 758: VLUGR2: a vectorizable adaptive grid solver for PDEs in 2D, *Assoc. Comput. Mach. Tran. Math. Software* 22 (1996) 302–328.
- [2] J.G. Blom, P.A. Zegelng, Algorithm 731: a moving-grid interface for systems of one-dimensional time-dependent partial differential equations, *Assoc. Comput. Mach. Trans. Math. Software* 20 (1994) 194–214.
- [3] F.H. Busse, Nonlinear properties of thermal convection, *Rep. Prog. Phys.* 41 (1978) 1929–1967.
- [4] G. Caginalp, B. McLeod, The interior transition layer for an ordinary differential equation arising from solidification theory, *Quart. Appl. Math.* 44 (1986) 155–168.
- [5] P. Davies, P. Blanchedeau, E. Dulos, P.D. Kepper, Dividing blobs, chemical flowers, and patterned islands in a reaction–diffusion system, *J. Phys. Chem.* 102 (1998) 8236–8244.
- [6] A. Doelman, W. Eckhaus, T.J. Kaper, Slowly-modulated two-pulse solutions in the Gray–Scott model. I. Asymptotic construction and stability, *SIAM J. Appl. Math.* 61 (2001) 1080–1102.
- [7] A. Doelman, W. Eckhaus, T.J. Kaper, Slowly-modulated two-pulse solutions in the Gray–Scott model. II. Geometric theory, bifurcations, and splitting dynamics, *SIAM J. Appl. Math.* 61 (2001) 2036–2062.
- [8] A. Doelman, R.A. Gardner, T.J. Kaper, Stability analysis of singular patterns in the 1D Gray–Scott model: a matched asymptotics approach, *Physica D* 122 (1998) 1–36.
- [9] A. Doelman, R.A. Gardner, T.J. Kaper, Large stable pulse solutions in reaction-diffusion equations, *Indiana Univ. Math. J.* 50 (2001) 443–507.
- [10] A. Doelman, R.A. Gardner, T.J. Kaper, A stability index analysis of 1D patterns of the Gray–Scott model, *Mem. Am. Math. Soc.* 155 (737) (2002), AMS, Providence, RI. ISSN 0065-9266.
- [11] A. Doelman, T.J. Kaper, Semi-strong pulse interactions in a class of coupled reaction-diffusion equations, *SIAM J. Appl. Dyn. Syst.* 2 (2003) 53–96.
- [12] A. Doelman, T.J. Kaper, P. Zegelng, Pattern formation in the one-dimensional Gray–Scott model, *Nonlinearity* 10 (1997) 523–563.
- [13] A. Doelman, H. van der Ploeg, Homoclinic stripe patterns, *SIAM J. Appl. Dyn. Syst.* 1 (2002) 65–104.
- [14] W. Eckhaus, On modulation equations of the Ginzburg–Landau type, in: *Proceedings of the Second International Conference on Industrial and Applied Mathematics ICIAM 91, 1992*, pp. 83–98.
- [15] W. Eckhaus, *Asymptotic Analysis of Singular Perturbations*, North-Holland, Amsterdam, 1979.
- [16] W. Eckhaus, *Studies in Nonlinear Stability Theory*, Springer-Verlag, New York, 1965.
- [17] P. Gray, S.K. Scott, Autocatalytic reactions in the isothermal, continuous stirred tank reactor: isolas and other forms of multistability, *Chem. Eng. Sci.* 38 (1983) 29–43.
- [18] P. Gray, S.K. Scott, Autocatalytic reactions in the isothermal, continuous stirred tank reactor: oscillations and instabilities in the system $A + 2B \rightarrow 3B$, $B \rightarrow C$, *Chem. Eng. Sci.* 39 (1984) 1087–1097.
- [19] A. Hagberg, E. Meron, T. Passot, Phase dynamics of nearly stationary patterns in activator–inhibitor systems, *Phys. Rev. E* 61 (2000) 6471–6476.
- [20] D. Haim, G. Li, Q. Ouyang, W.D. McCormick, H. Swinney, A. Hagberg, E. Meron, Breathing spots in a reaction-diffusion system, *Phys. Rev. Lett.* 77 (1996) 190.
- [21] P. Hirschberg, E. Knobloch, Zigzag and varicose instabilities of a localized stripe, *Chaos* 3 (1993) 713–721.
- [22] C. Laing, W. Troy, Two-bump solutions of Amari-type models of neuronal pattern formation, *Physica D* 178 (2003) 190–218.

- [23] K.J. Lee, H.L. Swinney, Lamellar structures and self-replicating spots in a reaction–diffusion system, *Phys. Rev. E* 51 (1995) 1899–1915.
- [24] K. Lee, H. Swinney, Replicating spots in reaction–diffusion systems, *Int. J. Bifurcat. Chaos* 7 (1995) 1149–1158.
- [25] K.-J. Lin, W.D. McCormick, J.E. Pearson, H.L. Swinney, Experimental observation of self-replicating spots in a reaction–diffusion system, *Nature* 369 (6477) (1994) 215–218.
- [26] M. Mimura, M. Nagayama, Nonannihilation dynamics in an exothermic reaction–diffusion system with mono-stable excitability, *Chaos* 7 (1997) 817–826.
- [27] D.S. Morgan, A. Doelman, T.J. Kaper, Stationary periodic orbits in the 1D Gray–Scott model, *Meth. Appl. Anal.* 7 (2000) 105–150.
- [28] D.S. Morgan, On existence and stability of spatial patterns in an activator–inhibitor system exhibiting self-replication, Ph.D. Thesis, Boston University, 2001.
- [29] P.M. Morse, H. Feshbach, *Methods of Theoretical Physics*, McGraw-Hill, New York, 1953.
- [30] C. Muratov, V. Osipov, Static spike autosolitons in the Gray–Scott model, *J. Phys. A* 33 (2000) 8893–8916.
- [31] C. Muratov, V. Osipov, Stability of the static spike autosolitons in the Gray–Scott model, *SIAM J. Appl. Math.* 62 (2002) 1463–1487.
- [32] N. Nefedov, Contrast structures of spike type in nonlinear singularly perturbed elliptic equations, *Russ. Acad. Sci. Doklady Math.* 46 (1993) 411–413.
- [33] Y. Nishiura, H. Fujii, Stability of singularly perturbed solutions to systems of reaction–diffusion equations, *SIAM J. Math. Anal.* 18 (1987) 1726–1770.
- [34] Y. Nishiura, H. Suzuki, Nonexistence of higher dimensional stable Turing patterns in the singular limit, *SIAM J. Math. Anal.* 29 (1998) 1087–1105.
- [35] Y. Nishiura, D. Ueyama, A skeleton structure for self-replication dynamics, *Physica D* 130 (1999) 73–104.
- [36] Y. Nishiura, D. Ueyama, Spatio-temporal chaos for the Gray–Scott model, *Physica D* 150 (2001) 137–162.
- [37] J.E. Pearson, Complex patterns in a simple system, *Science* 261 (1993) 189–192.
- [38] V. Petrov, S.K. Scott, K. Showalter, Excitability, wave reflection, and wave splitting in a cubic autocatalysis reaction–diffusion system, *Phil. Trans. Roy. Soc. London, Ser. A* 347 (1994) 631–642.
- [39] H.V.D. Ploeg, Personal communication.
- [40] W.N. Reynolds, J.E. Pearson, S. Ponce-Dawson, Dynamics of self-replicating patterns in reaction diffusion systems, *Phys. Rev. Lett.* 72 (1994) 2797–2800.
- [41] W.N. Reynolds, S. Ponce-Dawson, J.E. Pearson, Self-replicating spots in reaction–diffusion systems, *Phys. Rev. E* 56 (1997) 185–198.
- [42] A.M. Turing, The chemical basis of morphogenesis, *Phil. Trans. Roy. Soc. London, Ser. B* 237 (1952) 37–72.
- [43] D. Walgraef, *Spatio-temporal Pattern Formation: With Examples from Physics, Chemistry, and Materials Science*, Springer-Verlag, New York, 1997.
- [44] J. Wei, Pattern formation in two-dimensional Gray–Scott model: existence of single-spot solutions and their stability, *Physica D* 148 (2001) 20–48.
- [45] J. Wei, M. Winter, Existence and stability of multi-spot solutions of the Gray–Scott model in R^2 , *Physica D* 176 (2003) 147–180.
- [46] J. Wei, M. Winter, Asymmetric spotty patterns for the Gray–Scott model in R^2 , *Stud. Appl. Math.* 110 (2003) 63–102.
- [47] S. Wolfram, *The Mathematica Book*, 4th ed., Wolfram Media/Cambridge University Press, 1999.